RSC Advances

PAPER

View Article Online
View Journal | View Issue

Cite this: *RSC Adv.*, 2026, **16**, 10966

A novel method of shortening the pathway between surface reactive oxygen species and organic receptors under surface lattice metal atom substitution over HZSM-5 for intensifying catalytic oxidation CH_2Cl_2

Jian Li, *[a] Mengjie Zhao,[ab] Ziyi Song,[ab] Yingjie Shi,[a] Tianshan Xue,*[a] Jiayu Huang,[a] Hongchang Wang,[a] Jinwei Zhu,[a] Yutao Cui[a] and Yuling Tan[a]

Efficient catalytic oxidation of chlorine-containing volatile organic compounds (CVOCs) is a major research focus, but challenges include chlorine resistance, high HCl generation rates and maintaining high conversion rates. To overcome these technical bottlenecks, a series of transition metal (Cu, Cr, Fe, Co and Mn)-doped ZSM-5 molecular sieves were successfully synthesized with lattice Si^{4+} ions substituted by a one-step hydrothermal process. CH_2Cl_2 (DCM) served as a probe molecule to evaluate catalytic oxidation performance, while advanced physicochemical characterization elucidated the catalytic reaction, chlorine resistance and HCl generation mechanisms over the doped HZSM-5. The results show that *in situ* targeted substitution of transition metal atoms over HZSM-5 on the lattice Si^{4+} sites can induce the emergence of the twinning between the surface lattice single metal atoms and surface reactive oxygen nearby. Compared with supported HZSM-5, metal-doped HZSM-5 has greater catalytic performance and better resistance to chlorine poisoning and Cl deposition, due to the shortened pathway of surface reactive oxygen migration between surface reactive oxygen species and organic receptors, which can play an important role in catalytic oxidation and facilitate deep oxidation and inhibit Cl deposition. Mn- and Cr-doped HZSM-5 catalysts possess a high content of surface active oxygen, relatively high transfer ability, relatively high low-temperature reducibility and more appropriate intensities and quantities of surface Brønsted acids and Lewis acids, which results in a higher rate of DCM conversion, accompanied by relatively high CO_2 generation rate and HCl generation rate, as well as a strong ability to inhibit Cl deposition. Furthermore, the different synergistic reaction routes of DCM oxidation over metal-doped HZSM-5 are also proposed. We believe that this work can provide new insights into the design of catalysts for purifying CVOCs.

Received 19th August 2025
Accepted 16th November 2025

DOI: 10.1039/d5ra06126a

rsc.li/rsc-advances

1. Introduction

Volatile organic compounds (VOCs) are highly toxic or have strongly unpleasant odours and are thus among the main components of atmospheric pollution.[1] Among VOCs, chlorine-containing volatile organic compounds (CVOCs) easily generate other persistent organic byproducts.[2,3] The direct discharge of large amounts of untreated CVOCs poses a significant threat to both the environment and human health. Currently, the main methods for treating CVOCs include adsorption, absorption, condensation, membrane separation, incineration, biodegradation, photocatalytic oxidation, and catalytic combustion.[4,5] Among these methods, the catalytic oxidation technique, which has many advantages, such as low energy consumption, process safety and high selectivity, is widely recognized as an effective approach for treating VOCs.[6,7]

In recent years, many studies on the catalytic oxidation of CVOCs have been reported. Zha *et al.*[8] prepared Pd/TiO_2, Pt/TiO_2, and Rh/TiO_2 catalysts to study their catalytic oxidation of chlorobenzene (CB). They reported that Ru/TiO_2 catalysts exhibit better catalytic activity and higher CO_2 selectivity, with the lowest yield of polychlorinated byproducts. Z. Zhiwei *et al.*[9] prepared CuO/CeO_2 bimetallic oxide catalysts to study their ability to catalyse the oxidation of 1,2-dichlorobenzene. The experimental results show that 25%-$CuO@CeO_2$ has good low-temperature catalytic degradation performance. Additionally, the catalytic degradation efficiency can remain above 90% even

[a]*State Key Laboratory of Environmental Criteria and Risk Assessment, Chinese Research Academy of Environmental Sciences, Beijing 100012, China. E-mail: 1059151202@qq.com; xue.tianshan@craes.org.c; Fax: +15028692572; +15201444184; Tel: +15028692572; +15201444184*

[b]*School of Chemical and Environmental Engineering, China University of Mining and Technology (Beijing), Beijing 100083, China*

after six cycles of use. Even so, the CVOC catalysts studied here can achieve a better rate of catalytic conversion, but the deactivation due to carbon deposition and poisoning by chlorine are not prevented, which can lead to the formation of more toxic byproducts. Therefore, increasing the resistance of catalysts to chlorine poisoning and carbon deposition is currently an important direction in catalyst research. Therefore, some researchers have used many methods, such as changing metal elements, blending multiple metal oxides, optimizing the catalyst structure, and adjusting the lattice structure, to increase the content of reactive surface oxygen and mobility and improve the resistance to chlorine poisoning and carbon deposition. S. Ordóñez[10] compared the catalytic activity of Pd, Pt, Rh and Ru oxide-supported Al_2O_3 for DCM oxidation and reported that RuO/Al_2O_3 can exhibit better catalytic oxidation performance. L. Wenjun *et al.*[11] prepared Sn-doped Ru/TiO_2 to improve surface lattice defects and facilitate surface active content and mobility. Long *et al.*[12] discovered that Mn–Ce–Zr mixed-doped metal oxides can exhibit excellent redox ability, possess abundant surface active oxygen and have a high Cl removal capacity. Additionally, several three-dimensional macroporous catalysts can also be synthesized successfully to further improve the surface redox ability for deep oxidation and resistance to chlorine poisoning. Dai *et al.*[13] analysed the catalytic performance of CeOx-supported Ru_yM (M = Au, Pd and Pt) catalysts for the catalytic oxidation of trichloroethylene, which can exhibit good catalytic oxidation ability, but some chlorinated organic byproducts were produced. Wu *et al.*[14] prepared a series of CoCuOx@MOx (M = Nb, Ti and Ce) catalysts. The results reveal that CoCuOx@MOx core–shell structure catalysts can possess better surface acidity and surface oxygen mobility, which intensifies the resistance to chlorine poisoning. However, the method of removing Cl from the surfaces of the above catalysts involves Cl_2 *via* the Deacon reaction ($4HCl + O_2 \rightarrow 2Cl_2+2H_2O$), which is an extremely toxic substance that is harmful to humans. Therefore, changing the removal method of surface Cl from catalysts is highly important. HCl acts as one of the final products of Cl in the catalytic oxidation of CVOCs; it is nontoxic and can be easily washed, alkali washed and removed in other ways. Hence, HCl is the best destination for Cl in CVOCs, which need a certain hydrogen component.[2] Thus, the appropriate content and intensity of surface Brønsted acids on the catalyst are needed.[15]

Zeolite Socony Mobil–5 (ZSM-5), a typical MFI structure, has been widely applied in catalysis because of its advantages, such as adjustable hydrophobicity, high surface acidity, and high thermal stability.[16,17] It has a relatively high resistance to HCl corrosion, reduces the loss of elements such as Al in the lattice, and can adapt to complex and changing industrial exhaust gas environments. Additionally, the content and intensity of surface Brønsted acids and Lewis acids can be adjusted and reconstructed over ZSM-5, which has been popularly studied in the CVOC catalytic oxidation field in recent years. However, the redox ability of ZSM-5 is weaker than that of metal oxide catalysts. To improve the redox ability and synergistically improve the acid distribution and surface oxidation reducibility, many methods, such as improving the mesoporous structure, loading some metals and their oxides, and ion exchange coordination, have been used for ZSM-5 modification. Aranzabal *et al.*[18,19] reported that HZSM-5 has better catalytic stability than H-MOR and H-BETA do, and the carbon deposition and loss of Al are lower, resulting in greater resistance to HCl corrosion. S. Scirè *et al.*[20] discovered that Pt/HZSM-5 has better catalytic activity and produces fewer byproducts, such as polychlorinated biphenyl (PhClx). This is due to the strong surface acidity of the HZSM-5 molecular sieve, which is conducive to the adsorption of chlorobenzene molecules and the fracture of the C–C1 bond. Moreover, the pore size of HZSM-5 is smaller than the molecular size of PhClx, and its type selection limits the formation of PhClx. Rivas B.d. *et al.*[21] prepared a series of CeO_2/HZSM-5 materials for dichloroethane oxidation. The results show that there is a synergistic catalytic effect between the surface oxygen component of CeO_2 and the surface acidity of HZSM-5, which significantly improves the selectivity of CO_2 and HCl. Han Rui and Liu Qingling's research group[22] studied the catalytic oxidation of dichloromethane (DCM) by single-atom Pt and Co_3O_4 co-modified with HZSM-5. The results show that the interaction between single-atom Pt and Co oxide increases the surface oxygen site concentration and increases the migration ability of the oxygen components. Moreover, the addition of HZSM-5 for surface acid adsorption and cleavage jointly improved the catalytic degradation ability of DCM and increased the CO_2 yield and HCl selectivity, resulting in a smaller amount of byproducts. To improve the catalytic oxidation ability and chlorine resistance further, Weng *et al.*[23,24] prepared a series of $Mn_xCe_{1-x}O_2$/HZSM-5 catalysts for chlorobenzene oxidation, and the acidity and reactive oxygen species on the surface of HZSM-5 were significantly improved. Additionally, Dai *et al.*[25] and Fei *et al.*[26] separately prepared CeO_2@HZSM-5 and Co_3O_4@ZSM-5 core–shell catalysts for the catalytic oxidation of CVOCs. The results reveal that the deep oxidation ability and chlorine resistance are increased, but a certain amount of Cl_2 gas is generated on the surfaces of CeO_2 and Co_3O_4. Owing to its unique pore structure, surface acidity and other characteristics, the ZSM-5 molecular sieve can organically combine with surface active components, synergistically promote the deep oxidation capacity and removal of Cl components, and improve the selectivity of HCl; however, the formation of Cl_2 cannot be avoided. Hence, how to further reduce the catalytic oxidation temperature of CVOCs over ZSM-5, improve the selectivity and generation rates of CO_2 and HCl, and reduce or prevent the generation of chlorine-containing byproducts is the key problem that needs to be solved at present.

The key to solving the above problems is to improve the combination efficiency of the surface H component and Cl component and enrich the surface with reactive oxygen species, which can shorten the time for surface reactive oxygen species to reach the organic adsorption sites, increase the oxidation reaction rate, reduce the catalytic reaction temperature and reduce the degree of polymerization and chlorination of organic products. To date, research on the active oxygen components that are directly produced at the molecular sieve adsorption site and immediately oxidized by organisms after adsorption and

the dissociation of VOC molecules is insufficient. To achieve the immediate oxidation of organic matter at acidic sites and promote the formation of HCl, our research group proposes a new approach for designing CVOC catalysts on ZSM-5. The lattice Si^{4+} ions of ZSM-5 are anchored *in situ* for substitution by transition metal atoms, which possess better redox ability and different ion radii, charge performance and coordination environments. Owing to the differences in radius, valence state, electronegativity and other properties between transition metal ions and the lattice Si^{4+} of ZSM-5, the ZSM-5 molecular sieve lattice is distorted, and more defects are generated, which can induce the generation of more surface oxygen vacancies, increase the number of active oxygen atoms, and promote an increase in redox ability. Additionally, the surface acidity changes due to the difference in electronegativity and valence state between the substituted metal ions, which optimizes the molecular adsorption behaviour of CVOCs, further promotes the fracture of C–H, C–C and C–Cl bonds, and increases the decomposition rate of CVOCs. The generated organic free radicals can be immediately attacked and oxidized by the surrounding active oxygen components, which shortens the attack time for active oxygen components. Moreover, the attack path of reactive oxygen species is also shortened, thereby improving the oxidation rate and the removal ability of CVOCs and reducing carbon deposition. In addition, the chlorine component can combine with the H surface component to form HCl, which can be removed, thereby reducing chlorine poisoning and greatly improving HCl yield and selectivity. To confirm the above design, our research group studied the catalytic performance of Mn-, Cu-, Cr-, Fe- and Co-doped ZSM-5 for the catalytic oxidation of *n*-hexane. The results show that metal doping coupling can synergistically improve the surface acidity and redox capacity of ZSM-5, in which the surface B/L acid distribution is optimized and the catalytic cracking and deep oxidation of organic volatiles are improved. Moreover, metal-doped ZSM-5 also has good water resistance.[27] However, the catalytic performance and mechanism of CVOC oxidation over metal-doped ZSM-5 are not clear.

In this work, several transition metals (Cu, Cr, Fe, Co and Mn) were anchored *in situ* to the substituted lattice Si^{4+} of HZSM-5 by a hydrothermal process. Additionally, DCM was selected as a probe molecule for CVOCs because it is widely used as an organic solvent in various industries, such as pharmaceuticals, rubber, and coating production, and it is harmful to human health and the atmosphere. Furthermore, advanced characterization methods were used to analyse the physicochemical properties of the prepared catalysts, and the rates of CO_2, CO, HCl, Cl_2 and organic byproduct generation were investigated. The influence of the metal type and doping amount on the catalytic oxidation of DCM was explored. Moreover, the reaction route and Cl removal mechanism were studied and proposed. We believe that this work provides valuable insights for further studies on the catalytic oxidation of CVOCs by ZSM-5 catalysts; moreover, the obtained data support further research and potential industrial applications of heteroatomic mesoporous ZSM-5 catalysts for CVOC removal.

2. Experimental

2.1 Catalyst preparation

A certain amount of N (N stands for Fe, Cu, Cr or Co nitrate or potassium permanganate) was added to a certain amount of deionized water dissolved in 10 mL of 30% ammonia aqueous solution (AR, 25%, Shanghai Zhanyun Chemical Reagent Factory) and a certain amount of ethylenediaminetetraacetic acid (EDTA), and the resulting solution was denoted solution A. Silicic acid (AR, supplied by Wengjiang Reagent), aluminium hydroxide, sodium hydroxide, deionized water, tetrapropylammonium hydroxide (TPAOH, 25 wt%, Sigma Aldrich) and the abovementioned solution A were added to a 200 mL polytetrafluoroethylene reactor liner. The molar ratio of each component was as follows: $M : SiO_2 : Al_2O_3 : H_2O : Na_2O : TPAOH = 0.5 : 100 : 2 : 2000 : 12 : 20$. After stirring in a water bath at 60 °C for 2 h, the reactor lining was put into a stainless steel sleeve, crystallized in a 160 °C oven for 18 h and then cooled to room temperature after removal. The crystallized product was filtered, washed until neutral, dried for 6 h, and roasted in a muffle furnace at 550 °C for 5 h to obtain M-ZSM-5 with a doping amount of 0.5% (M/Si atomic percentage). Afterwards, M-ZSM-5 was stirred in a 5% NH_4Cl solution at 80 °C for 2 h to obtain the molecular sieve M-HZSM-5 (M = Fe, Cu, Cr, Co and Mn). According to the above the 1.2% Cr-HZSM-5 was also prepared in this work. At the same time, the supported Cr/HZSM-5 was prepared in the impregnation method.

2.2. Catalyst characterization

The synthesized samples were systematically characterized by X-ray diffraction (XRD), N_2 adsorption and desorption, scanning electron microscopy (SEM), DRS UV-Vis absorption spectroscopy, X-ray photoelectron spectroscopy (XPS), temperature-programmed reduction of hydrogen (H_2-TPR), temperature programmed desorption of O_2 (O_2-TPD), temperature-programmed desorption of NH_3 (NH_3-TPD), and pyridine adsorption Fourier transform infrared (Py-IR) spectroscopy. The detailed information is expressed in the SI.

2.3. Catalytic activity

A total of 0.3 g zeolite catalyst was placed into a quartz tube, both ends were fixed with passivated quartz asbestos, and the quartz tube was placed in a tubular heating furnace. Under a 200 ml min^{-1} nitrogen gas flow, the reactor was heated to 150 °C at a heating rate of 5°C min^{-1} and held at that temperature for 1 h to eliminate water and other impurities adsorbed on the surface of the catalyst. The tube furnace gas was then switched to a stable concentration of DCM, and the programmed heating catalytic reaction was carried out under the conditions of a total gas flow rate of 200 ml min^{-1} and a mass airspeed of 40 000 mL g^{-1} h. The tube furnace was heated at a rate of 5°C min^{-1} to preset reaction temperatures of 150 °C, 200 °C, 250 °C, 300 °C, 350 °C, 400 °C and 450 °C. The organic components in the exhaust gas were analysed online *via* GC-MS; CO and CO_2 concentrations were detected by an

infrared detector, and HCl and Cl_2 were detected by a portable gas detector.

The DCM conversion, CO_2 selectivity, HCl selectivity, and $CHCl_3$ production rates were calculated as follows:

$$X_{CH_2Cl_2}(\%) = \frac{[CH_2Cl_2]in - [CH_2Cl_2]out}{[CH_2Cl_2]in} \times 100 \quad (2.1)$$

$$Y_{CH_3Cl}(\%) = \frac{[CH_3Cl]out}{[CH_2Cl_2]in} \times 100 \quad (2.2)$$

$$CO_2\ \text{yield}(\%) = \frac{[CO_2]out}{[CH_2Cl_2]in} \times 100 \quad (2.3)$$

$$CO\ \text{yield}(\%) = \frac{[CO]out}{[CH_2Cl_2]in} \times 100 \quad (2.4)$$

$$CO_2\ \text{selectivity}(\%) = \frac{[CO_2]out}{[CH_2Cl_2]in - [CH_2Cl_2]out} \times 100 \quad (2.5)$$

$$CO\ \text{selectivity}\ (\%) = \frac{[CO]out}{[CH_2Cl_2]in - [CH_2Cl_2]out} \times 100 \quad (2.6)$$

$$Cl_2\text{yield}(\%) = \frac{[Cl_2]out}{[CH_2Cl_2]in} \times 100 \quad (2.7)$$

$$Cl_2\ \text{selectivity}(\%) = \frac{[Cl_2]out}{[CH_2Cl_2]in - [CH_2Cl_2]out} \times 100 \quad (2.8)$$

$$HCl\text{yield}(\%) = \frac{[HCl]out}{2 \times [CH_2Cl_2]in} \times 100 \quad (2.9)$$

$$Y_b(\%) = X_{CH_2Cl_2} - CO_2\ \text{yield} - CO\ \text{yield} - Y_{CH_3Cl} \quad (2.10)$$

$$Y_{Cl\text{-}b}(\%) = X_{CH_2Cl_2} - Cl_2\ \text{yield} - HCl\ \text{yield} - \frac{1}{2}Y_{CH_3Cl} \quad (2.11)$$

In the above equations, $[CH_2Cl_2]$in and $[CH_2Cl_2]$out are the inlet and outlet concentrations, respectively. $[CH_3Cl]$out, $[CO_2]$out, $[Cl_2]$out, and [HCl]out are the outlet concentrations of CH_3Cl, CO_2, Cl_2 and HCl, respectively. $X_{CH_2Cl_2}$ is the catalytic conversion of CH_2Cl_2, %; Y_{CH_3Cl} is the yield of CH_3Cl, %; Y_b is the sum of undetected organic components (including catalyst surface deposited carbon), %; and $Y_{Cl\text{-}b}$ is the sum of undetected chlorine-containing components (including catalyst surface deposited chlorine), %.

3. Results and discussion

3.1 Characterization of the prepared catalysts

3.1.1 XRD. The crystal structures of the different M-HZSM-5 catalysts (M = Cu, Cr, Fe, Co and Mn) were characterized by XRD, and the XRD patterns are shown in Fig. 1(a). The 2θ values of the catalysts exhibited diffraction peaks at 7.9°, 8.8°, 23.1°, 23.9° and 24.4°, which are similar to the positions of the characteristic peaks of ZSM-5 (PDF#45-0120) in the standard card and correspond to the (101), (200), (501), (303) and (133) crystal planes, respectively, indicating that the ZSM-5 zeolites were successfully synthesized.[22] Furthermore, no characteristic diffraction peaks corresponding to metal oxides were observed, indicating that the metal oxides were highly dispersed on the surface of the catalysts or incorporated into the crystal lattice of ZSM-5.[28] Fig. 1(b) indicates that the characteristic diffraction peaks of M-HZSM-5 moved in the low-angle region, which implies that the crystal plane spacing increased after metal doping. This increase may have been due to the difference in radius between the metal ions and Si^{4+}/Al^{3+}, resulting in longer M–O bonds than Si–O bonds; metal ions entering the zeolite skeleton caused the molecular sieve unit cell to increase in size, increasing the crystal plane spacing. The above results indicate that the metal ions can be successfully doped into the molecular sieve skeleton and substitute for some Si^{4+} or Al^{3+} ions.[29]

3.1.2 ^{29}Si MAS-NMR and DRSUV-Vis. To further confirm whether the transition metal atoms were incorporated into the lattice framework of HZSM-5, ^{29}Si MAS-NMR and DRS UV-Vis were performed for all the prepared catalysts. The results are shown in Fig. S2 and Fig. 2. The peaks at −104 ppm and −16 ppm appear for all the samples and are assigned to the $Q^3[YOSi(OSi)_3]$ and $Q^4[Si(OSi)_4]$ resonance peaks, respectively.[30] $Q^3[YOSi(OSi)_3]$ indicates that one Si atom is encircled by three Si atoms and one Y atom, where Y stands for the H or metal elements, and $Q^4[Si(OSi)_4]$ indicates that one Si atom is encircled by four Si atoms.[30,31] As shown in Table S1, compared with that of the HZSM-5 peak, the percentage of the Q^3 peak increased slightly with transition metal atom doping, and the Q^3/Q^4 area ratio increased from 0.034 to 0.048–0.086, implying that the chemical environment around Si changed. This phenomenon is induced by metal ion substitution at the Si sites.[30] SiO_4 can be deformed with the substitution of metal ions with ionic radii differing from those of Si^{4+} in the framework, resulting in a change in the chemical environment around Si, which agrees with recent studies.[32,33]

Fig. 2 shows the DRSUV-Vis absorption spectra of all the M-HZSM-5 catalysts. There were significant differences in the DRS UV-Vis absorption spectra of the different metal-doped HZSM-5 materials. The absorption peaks near 265 nm and 360 nm for the Cr-HZSM-5 zeolite corresponded to the charge transition of framework O(2p) → tetracoordinate Cr^{6+} ($3d^0$), indicating that many Cr^{6+} ions were doped into the HZSM-5 lattice. The weak absorption peaks at 400∼500 and 600∼700 nm could belong to octahedral Cr^{3+},[34] indicating that Cr mainly existed in the skeleton of the molecular sieve in the form of Cr^{6+} and that there was a small amount of extra skeletal Cr in the form of Cr_2O_3 or other forms. A sharp peak at 233 nm was observed for Cu-HZSM-5, corresponding to the electron transition of framework O(2p) → tetradentate Cu^{2+}(3d), indicating that Cu was successfully incorporated into the skeleton of the zeolite.[30] The signal peak of Mn-HZSM-5 at approximately 265 nm was attributed to the electron transition of the skeleton O(2p) → Mn^{3+}(3d)/Mn^{2+}(3d).[35] Fe-HZSM-5 had characteristic peaks at approximately 250 nm, which belong to tetrahedrally coordinated Fe^{3+}.[36] The characteristic absorption peak at 300–400 nm in the ultraviolet spectrum of Co-HZSM-5 was attributed to tetrahedrally coordinated Co^{3+}. According to the literature,[37] Co^{2+} produces three characteristic absorption peaks in the UV-Vis spectral range of 500–700 nm, but no obvious absorption

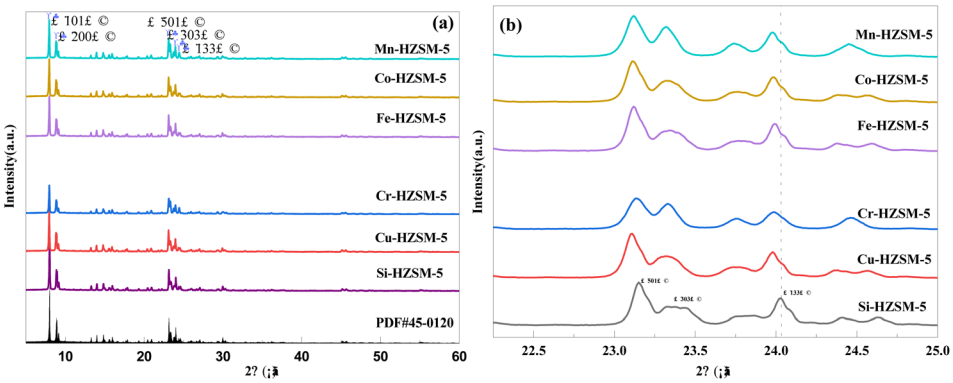

Fig. 1 (a) XRD patterns of all the catalysts and (b) the enlarged part XRD patterns of all the catalysts.

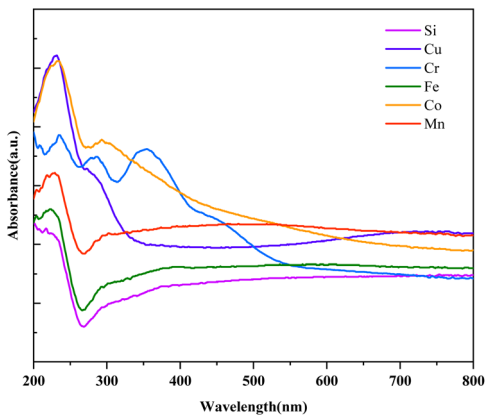

Fig. 2 DRS UV-Vis spectra of all the catalysts.

peaks were observed in this range, indicating that the Co in the catalysts existed mainly in the form of CoO_x and that only a very small amount of Co was doped into the skeleton of the molecular sieve. Furthermore, the above results revealed that the one-step hydrothermal synthesis method successfully achieved monometallic isomorphism of the transition metals Cu, Cr, Fe, Co and Mn for MFI-type zeolites and that each metal ion entered the molecular sieve skeleton, whereas some metals that did not participate in crystallization remained on the surface or in the pores of the zeolite in the form of oxides.

3.1.3 BET. Fig. 3 displays the isothermal adsorption and desorption curves and pore size distributions of all the catalysts. All the prepared catalysts showed similar texture characteristics, and the N_2 adsorption–desorption isotherms of all the prepared catalysts corresponded to type IV isotherms with H_4 hysteresis loops, demonstrating that microporous and mesoporous structures coexisted in the catalysts.[38] However, as shown in Fig. 3(b), the pore size of the catalysts was concentrated in the range of <2 nm, and some mesopores in the range of 2–4 nm were also observed, which may be due to the irregular accumulation of nanocrystals in the molecular sieve.[25] The textural property parameters of all the prepared catalysts are displayed in Table 1. The specific surface areas of all the catalysts were in the range of 330∼367 m^2 g; moreover, the reduction in specific surface area after Cr doping may be due to the deposition of some metal oxides on the outer surface of the molecular sieve or part of its pores, resulting in pore blockage and a decrease in the overall specific surface area.[39] Additionally, the above findings and the XRD and DRS UV-Vis results collectively indicate that the incorporation of metal ions with different radii into the HZSM-5 framework can change the unit cell structure of HZSM-5 and slightly change the specific surface area and pore volume of HZSM-5.

3.1.4 XPS. To investigate the valence state distribution of the substitution metal elements, XPS was performed, as shown in Fig. S3. The Co $2p_{3/2}$ spectra are composed of three peaks at 780.8 eV, 782.0 eV and 786.9 eV corresponding to Co^{3+}, Co^{2+} and the satellite peak of Co^{2+}($Co_{sat.}^{2+}$), respectively.[40] Notably, the intensity of the Co^{2+} signal is much stronger than that of the Co^{3+} signal, implying that Co exists mainly in the form of Co^{2+}. Furthermore, the binding energy of Co $2p_{3/2}$ shifted to a position higher than those of reported Co oxides, such as CoO at 780.4 eV, Co_2O_3 at 779.4 eV and Co_3O_4 at 779.8 eV, which is due to the strong interaction between the Co species and ZSM-5; alternatively, Co atoms may be incorporated into the ZSM-5 lattice. For Cr-HZ, Cr^{6+} (580.1 eV) and Cr^{3+} (577.7 eV) coexisted on ZSM-5.[41,42] In addition, the intense and sharp Mn $2p_{3/2}$ signal at 641.9 eV corresponds to Mn^{3+}, and the weak signals at 640.6 eV and 644.1 eV are attributed to Mn^{2+} and Mn^{4+},[43,44] respectively, indicating that Mn exists mainly in the form of Mn^{3+}. Moreover, the Mn 1s peak is split into two peaks with an energy difference of $\Delta E = 5.5$ eV (Fig. S3D). Generally, the ΔE values of the split Mn 1s peaks of MnO_2, Mn_2O_3 and MnO are approximately 4.7 eV, 5.3 eV and 6.0 eV, respectively.[45] The ΔE values of the split Mn 1s split peaks were similar to that of Mn_2O_3, indicating that most of the Mn atoms exist in a trivalent state. From Fig. S3E, Cu $2p_{3/2}$ is deconvoluted into three peaks at 933.1 eV, 936.3 eV and 942.3 eV, which are assigned to tetrahedral Cu^{2+}, octahedral Cu^{2+} and the satellite peak of Cu^{2+}, respectively.[46,47] The peak attributed to octahedral Cu^{2+} was very weak, implying that tetrahedral Cu^{2+} dominates and is incorporated into the ZSM-5 lattice and that octahedral Cu^{2+} can exist in the form of framework ions or extra-framework oxides. The peak position of the Fe $2p_{3/2}$ peak in the Fe 2p spectral peak of Fe-ZSM-5 appeared at 711.9 eV, and a satellite peak appeared at

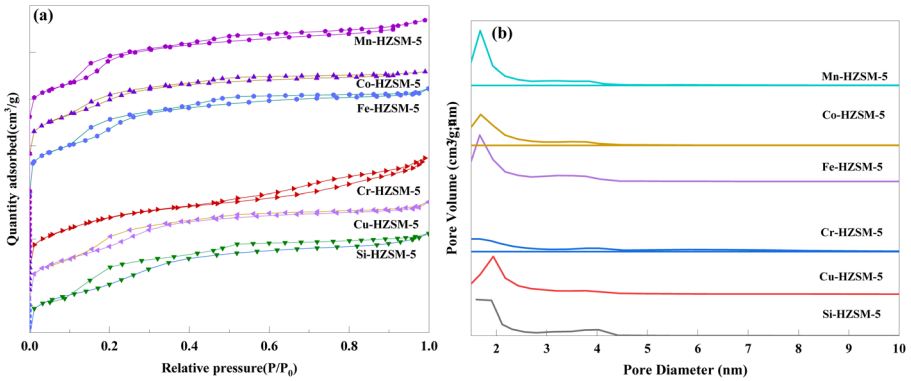

Fig. 3 (a) Pore size distributions and (b) pore size structures of all the catalysts.

Table 1 Specific surface area, pore volume and average pore size of each catalyst

Catalysts	Specific surface area ($m^2\ g^{-1}$)	Pore volume ($cm^3\ g^{-1}$)	Pore size (nm)
HZSM-5	343	0.11	2.34
Cu-HZSM-5	347	0.10	2.26
Cr-HZSM-5	330	0.10	2.43
Fe-HZSM-5	367	0.10	2.16
Co-HZSM-5	348	0.09	2.12
Mn-HZSM-5	354	0.11	2.19

717.1 eV. It can be attributed to the 2p spectral peak of Fe^{3+}, indicating that the valence state of Fe in the Fe-ZSM-5 prepared in this paper mainly exists as trivalent iron ions. However, the surface of Fe-ZSM-5 appeared white in this work. It indicates that neither Fe_2O_3 nor $Fe(OH)_3$ exists, further proving that Fe^{3+} is present within the framework of the molecular sieve.The above results agree with the DRS UV-Vis results.

3.1.5 NH_3-TPD and Py-FITR. The acidity of the zeolite surfaces was altered due to the *in situ* replacement of Si atoms in the zeolite backbone by transition metals with different ion radii and valence states.[30] To study the effect of the *in situ* introduction of different metal atoms on the surface acidity of the catalysts, the surface acidity of each catalyst was characterized by NH_3-TPD. Fig. 4(a) shows the NH_3-TPD curves of each catalyst. All curves were roughly divided into three temperature ranges, 100–200 °C, 200–350 °C and >350 °C, corresponding to the desorption of NH_3 adsorbed on weak acid sites, moderate-strength acid sites and strong acid sites on the surface of the catalysts, respectively.[37] In addition, the NH_3 desorption peak position and peak area represent the intensity and amount of acidity at acidic sites.[48] For almost all the metal-doped zeolite catalysts, the NH_3 desorption peaks in the weak, moderate-strength and strong acid ranges shifted to higher temperatures, the peaks became wider, and the area of the peaks increased. This change was attributed to the effect of metal coupling on regulating the surface acidity of HZSM-5. Notably, the coupling of different metals had different effects on the acidity of the molecular sieve surface, and the most prominent acidity changes were observed for Cr-HZSM-5 and Mn-HZSM-5, which had strong acid peaks at approximately 400 °C. In addition, the area of the weak acid peak of Cr-HZSM-5 changed the most, indicating that Cr coupling significantly increased the number of weakly acidic sites on the surface of the zeolite catalyst. Furthermore, to determine the type of acid centre, pyridine infrared analysis was performed on Cr-HZSM-5. Fig. 4(b) shows the infrared pattern of *in situ* pyridine for Cr-HZSM-5 in the range of 360–800 cm at 200 °C and 400 °C.

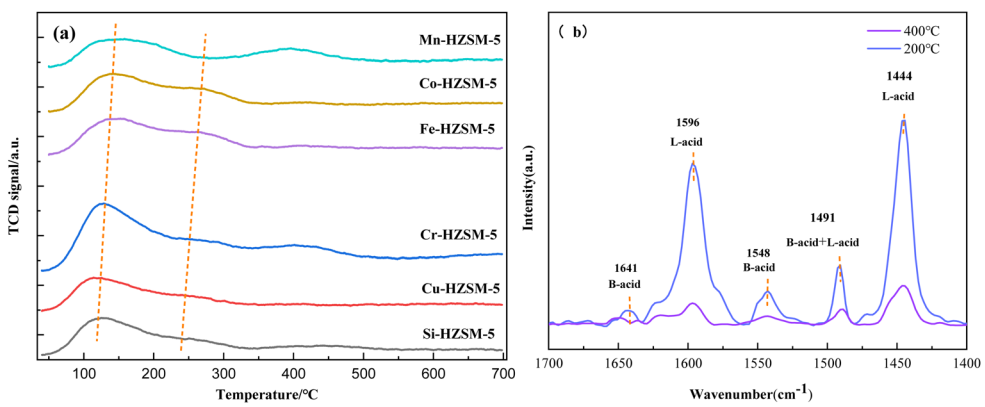

Fig. 4 (a) NH_3-TPD curves of each catalyst; (b) pyridine infrared spectra of each catalyst.

The bands at 1444 cm^{-1} and 1596 cm^{-1} were attributed to pyridine adsorption at Lewis acid sites, the bands at 1548 and 1641 cm^{-1} were attributed to pyridine adsorption at Brønsted acid sites, and the absorption peak at 1490 cm^{-1} was attributed to the combination of pyridine adsorbed at Lewis acid and Brønsted acid sites.[6,49] In comparison with HZSM-5(Fig. S3), the surface acidity was strengthened. Moreover, the peak aera of Lewis acid sites and Brønsted acid sites of Cr-HZSM-5 was larger than that of HZSM-5, indicating that the number of surface acid sites is improved after metal doping. From Fig. 4(b), both Brønsted acid and Lewis acids resulted in strong peak signals at 200 °C. When the temperature increased to 400 °C, the weak and moderate-strength acid sites adsorbed pyridine, but a certain amount of Brønsted and Lewis acids remained, and the B/L value increased from 0.27 to 0.40.[50] These results were consistent with the NH_3-TPD results.

The above results showed that the metal atoms Cu, Cr, Fe, Co and Mn replaced Si in the zeolite skeleton and that different metals presented different acidities on the surface of the zeolite due to differences in charge and electronegativity; in particular, Cr and Mn produced the most obvious changes in the acidity of the zeolite skeleton. Furthermore, the results showed that the surface acidity of HZSM-5 can be regulated by incorporating different metal elements into the skeleton.

3.1.6 O_2-TPD and H_2-TPR. To further explore the effects of metal atom doping of zeolite catalysts on the oxygen species on the catalyst surface, O_2-TPD was performed, and the TCD results are shown in Fig. 5(a). In the 50–800 °C temperature range, the oxygen desorption curve can generally be divided into three regions: less than 350 °C, 350–700 °C, and greater than 700 °C. In the curve, the oxygen desorption peak below 350 °C was due to the physical or chemical adsorption of α′-O (O_2^{2-}, O_2^-, O^-) on the surface of the molecular sieve, the desorption peak at 350–700 °C was due to surface lattice oxygen α-O (O^{2-}) generated by lattice defects, and the oxygen desorption peak at temperatures greater than 700 °C was due to body lattice oxygen β-O (O^{2-}) released from the crystal structure.[37,51] According to the relevant literature, the amount of oxygen present is proportional to the desorption peak area of the corresponding oxygen species.[52,53] The peak of the HZSM-5 zeolite catalyst at approximately 150 °C was attributed to the surface physical adsorption of oxygen species and defects. The results show that after the metal atoms are introduced into the skeleton, the desorption peaks of surface adsorbed oxygen species and surface lattice oxygen species for each catalyst became wider and larger; the catalysts also produced weak peaks at temperatures greater than 700 °C, and the Cr-HZSM-5 catalyst produced lattice oxygen species. The surface adsorbed oxygen content of each catalyst followed the order of Cr-HZSM-5 > Fe-HZSM-5 > Co-HZSM-5 > Cu-HZSM-5 > Mn-HZSM-5 >HZSM-5. The surface lattice oxygen content of each catalyst followed the order Cr-HZSM-5 > Fe-HZSM-5 > Co-HZSM-5 > Mn-HZSM-5 > HZSM-5 > Cu-HZSM-5. However, the migration temperature for surface adsorbed oxygen species and surface lattice oxygen species is lower in Mn-HZSM-5 than in other catalysts. The above results reveal that Cr-HZSM-5 and Mn-HZSM-5 possess better oxidizability due to the rich oxygen species of Cr-HZSM-5 and low-temperature migration capacity of Mn-HZSM-5.

The results showed that the surface adsorbed oxygen and surface lattice oxygen contents of each catalyst were increased by the *in situ* substitution of Cu, Cr, Fe, Co and Mn in HZSM-5. This finding indicated that the *in situ* introduction of different metal atoms caused the breakage of many Si–O or M–O bonds, resulting in many lattice defects, which captured oxygen from the ambient atmosphere and converted gaseous oxygen into more reactive oxygen species; moreover, the oxygen atoms in the lattice moved to the vacant sites due to the force vector. At the same time, new oxygen vacancies were formed, which increased the migration capacity of the oxygen species on the surface of the catalyst, thereby improving the redox performance of the catalyst.[51,54,55]

H_2-TPR was used to analyse all the catalysts to study the redox properties of the different metal-doped zeolite sieves, and the resulting TCD curves are shown in Fig. 5(b). HZSM-5 had a strong reduction peak at 430–700 °C, but the peak temperature was high, which was attributed to surface lattice oxygen. The reduction peaks of all the metal-doped zeolite catalysts moved towards lower temperatures. Generally, the lower the temperature of the reduction peak is and the larger the reduction peak is, the stronger the redox ability,[53] indicating that

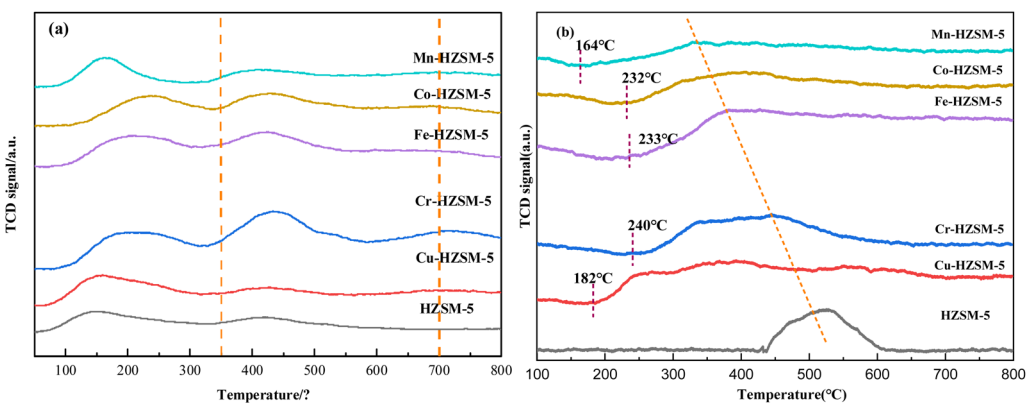

Fig. 5 (a) O_2-TPD curves of all the catalysts; (b) H_2-TPR curves of each catalyst.

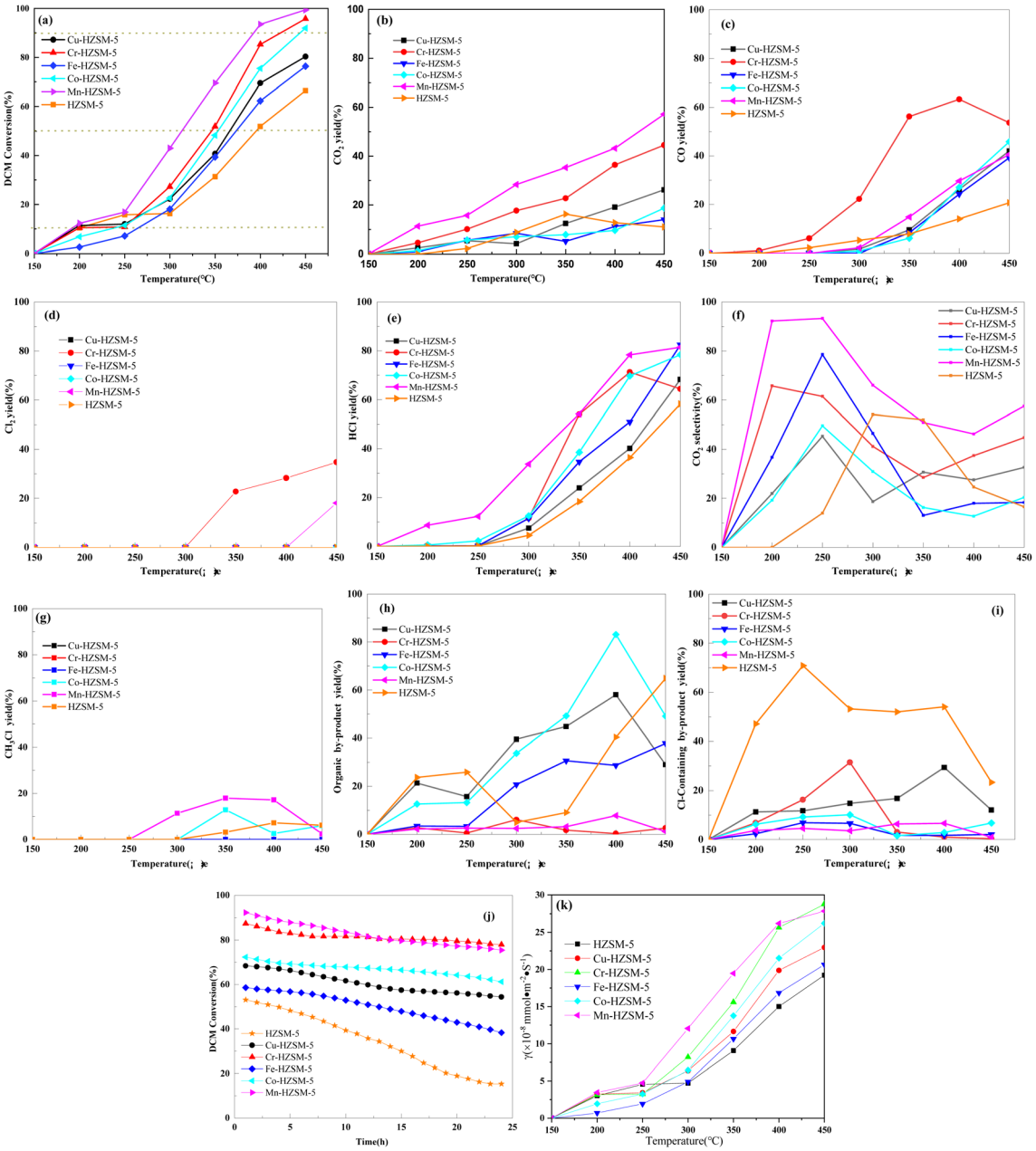

Fig. 6 (a) Catalytic activity, (b) CO_2 yields, (c) CO yields, (d) Cl_2 yields, (e) HCl yields, (f) CO_2 selectivity, (g) CH_3Cl yields, (h) orgnic by-product yields, (i) Cl-containing byproduct yields, (j) DCM conversions and (k) reaction rate per unit area of all the catalysts for DCM at different reaction temperatures.

strong redox reactions could promote the catalytic oxidation of DCM. Co-HZSM-5 has one broad peak at 260–450 °C, which is attributed to the overlapping peaks corresponding to the reduction of $Co^{3+} \rightarrow Co^{2+}$ at approximately 300 °C and the reduction of $Co^{2+} \rightarrow Co^{0}$ at approximately 420 °C.[56] Cu-HZSM-5 has a significant reduction peak at a low temperature of 250 °C that is associated with the reduction of $Cu^{2+} \rightarrow Cu^{+}$, a peak at 330–420 °C corresponding to the reduction of CuO, and a peak at high temperatures of 500–650 °C corresponding to the reduction of $Cu^{+} \rightarrow Cu^{0}$.[57] Fe-HZSM-5 presented a reduction peak of $Fe^{3+} \rightarrow Fe^{2+}$ at 365 °C. Mn-HZSM-5 formed a wide band with two overlapping peaks at 280–500 °C, which was attributed to the reduction of $Mn^{4+} \rightarrow Mn^{3+}$, and the obvious reduction peak centred at 380 °C corresponded to $Mn^{3+} \rightarrow Mn^{2+}$, indicating that the Mn^{3+} content in the molecular sieve was relatively high, which was consistent with the UV-Vis analysis results. Cr-HZSM-5 had a wide and strong peak at 330 °C, which was the reduction peak of $Cr^{6+} \rightarrow Cr^{3+}$, as well as a Cr_2O_3 reduction peak at 450 °C. After metal coupling, the reduction peak increased in area and shifted to lower temperatures, indicating that the addition of Cr, Mn, Cu, Fe and Co increased the reduction capacity of HZSM-5. The reduction capacity sequence was Cu-HZSM-5 > Cr-HZSM-5 > Mn-HZSM-5 > Co-HZSM-5 > Fe-HZSM-5 > HZSM-5, and the component content

and temperature of the reduction peak jointly affected the reduction effect of the catalyst. In addition, Mn-HZSM-5 had a low starting reduction temperature, indicating that Mn-HZSM-5 has a strong reduction ability at low temperatures.

3.2. Catalytic activity and selectivity

To investigate the effect of transition metal *in situ* coupling with ZSM-5 zeolites on the catalytic performance of DCM, Fig. 6 shows the DCM conversion and product distribution on different catalysts. As shown in Fig. 6(a) and (f), the catalytic activity of the HZSM-5 zeolites significantly improved after they were doped with different metals. According to the T_{50} (reaction temperature with conversion reaching 50%) and the reaction rates with different temperatures, the activity order of several catalysts was Mn-HZSM-5 (340 °C) > Cr-HZSM-5 (350 °C) > Co-HZSM-5 (355 °C) > Cu-HZSM-5 (360 °C) > Fe-HZSM-5 (365 °C) > HZSM-5 (395 °C). When the conversion rate was 90%, the catalytic activities of Mn-HZSM-5 and Cr-HZSM-5 were relatively high, both at 380 °C, and the catalytic activity of Co-HZSM-5 was 410 °C. Compared with Cr-HZSM-5, Mn-HZSM-5 had a lower number and strength of surface acid sites, but it had a lower initial reduction temperature and a higher low-temperature reduction ability, resulting in higher catalytic activity, whereas Cu-HZSM-5 had a greater oxidation reduction ability, and its catalytic activity was significantly lower than that of Mn and Cr-HZSM-5, which was related to its lower acidity and the presence of fewer acid sites. The results show that the catalytic oxidation process of halogenated hydrocarbons first involved C–Cl bond adsorption and fracture at the acid sites (B acid or L acid) and then oxidation by the surface oxygen component, indicating that surface acidity and redox performance are the main factors in the catalytic oxidation process of halogenated hydrocarbons, which is consistent with the results of this study. Notably, when the temperature increased to 200–250 °C, the DCM catalytic activity curves of Cu-HZSM-5 and Cr-HZSM-5 were relatively flat, and the catalytic activity curve of HZSM-5 was flat at 250–300 °C. From Fig. 6(e), no other catalysts produced HCl, except for the Mn-HZSM-5 and Co-HZSM-5 zeolites, which produced a small amount of HCl before 250 °C. The reason may be that the desorption temperature of HCl was not reached before 250 °C, and because the cracking rate of DCM was greater than the oxidation rate, more intermediate products were not further oxidized to occupy the activity centre, resulting in a decrease in catalytic activity. When the temperature increased to 300 °C, the trend of the DCM degradation curves of all the metal-doped zeolite catalysts increased significantly, and all the curves were greater than those of the HZSM-5 catalysts. This finding shows that metal doping improves the low-temperature redox performance of the surface of the molecular sieve catalyst. When the temperature reached 300 °C, the active components of all the metal-doped molecular sieve catalysts began to be activated, resulting in high catalytic oxidation activity.

The CO_2 and CO production rates shown in Fig. 6(b) and (c) reflect the mineralization rate of the catalyst. The COx production rates of all the metal-coupled HZSM-5 increased with increasing temperature. However, the CO_2 production rate of the HZSM-5 zeolite catalysts decreased at 350 °C, and the increase in the CO production rate increased, but it was lower than that of the other metal-doped zeolite catalysts. This is because the HZSM-5 zeolite has low redox properties, resulting in the production of intermediate transition products and CO that cannot be rapidly oxidized. After metal coupling, the redox properties of HZSM-5 were significantly enhanced, and the deep oxidation capacity was improved. At low temperatures, Mn-HZSM-5 resulted in greater CO_2 production, which was related to its lower initial reduction temperature. Both Cr-HZSM-5 and Mn-HZSM-5 had relatively high CO_2 production rates above 300 °C. The CO_2 production rate of the Mn-HZSM-5 catalyst reached 50%. Although the catalytic activity of the Mn-HZSM-5 zeolite catalyst was greater than that of the Cr-HZSM-5 zeolite catalyst, the CO production rate of the Cr-HZSM-5 zeolite catalyst was the highest, which was related to its greater number of acid sites. With increasing temperature, the cracking ability ofacid sites was increased, and the presence of a greater number ofacid sites resulted in the production of more byproducts. The redox ability of Cr-HZSM-5 was insufficient to completely oxidize organic byproducts to CO_2, resulting in more CO. In addition, the Cr-HZSM-5 molecular sieve catalyst did not produce the byproduct CH_3Cl, which was related to more acid sites and more oxygen vacancies on the surface of the Cr-HZSM-5 molecular sieve catalyst. The presence of more acid sites can lead to the production of more byproducts, which is conducive to further dechlorination of CH_3Cl. More oxygen vacancies can provide more active oxygen components and increase the migration ability of oxygen components; improve the oxidation of intermediate transition products such as formaldehyde, methoxy, and formate; and reduce or prevent intermediate reactions between methoxy groups and HCl, which in turn leads to a lower yield of CH_3Cl and is undetectable. The distribution of the Cl_2, HCl and intermediate chlorine-containing byproducts of the Cu-HZSM-5 catalyst revealed that the reason why the Cu-HZSM-5 molecular sieve catalyst had high redox properties but not high catalytic activity was that there were many chlorine-containing byproducts on the catalyst surface, which decreased the catalytic activity of the catalyst surface. The catalytic activity of the Fe-HZSM-5 molecular sieve catalyst was slightly lower than that of the Cu-HZSM-5 molecular sieve catalyst, but the production rates of CO and CO_2 of the Cu-HZSM-5 molecular sieve catalyst were lower, whereas there were more intermediate organic products, which may be related to the formation of more carbon deposits on the surface of the Cu-HZSM-5 molecular sieve catalyst during the catalytic process. This result is also consistent with the results of the literature.[48]

The Cr-HZSM-5 and Mn-HZSM-5 catalysts had the highest catalytic activity, indicating that the strongly acidic checkpoints played an important role in the catalytic cracking of CVOCs. The experimental results are consistent with those in the literature.[6] Furthermore, the above results show that the *in situ* introduction of metals improved the acidity and redox properties of the catalysts. However, the order of catalytic activity cannot be consistent with the degree of oxidative activity or acidity alone,

and the greater the synergistic effect of acidity and reductivity is, the greater the catalytic activity.

Fig. 6(d) shows the Cl_2 production rates for each catalyst. No Cl_2 was detected among the catalytic DCM products of Co-HZSM-5, Cu-HZSM-5, Fe-HZSM-5 or HZSM-5. Because Cr-HZSM-5 has more surfactant oxygen components, the Cl_2 production temperature of Cr-HZSM-5 was 300 °C, which was lower than those of Ce-HZSM-5 and Mn-HZSM-5. The Cl_2 generation temperature of Mn-HZSM-5 was greater than that of the other samples at 400 °C. Cl_2 formation was not detected in Fe-HZSM-5. Furthermore, Cl balance calculations indicated that Fe-HZSM-5 had good HCl selectivity.

Fig. 6(e) shows the distribution of HCl production rates for each catalyst. The HCl selectivity of each zeolite catalyst after metal doping was greater than that of HZSM-5, indicating that the doped metals increased the acid strength and the number of acid sites on the catalyst surface and enhanced the initial cleavage of C–Cl in DCM. The HCl production rate of the Mn-HZSM-5 zeolite catalyst starts at 200 °C, and the HCl production rate reached 80% at 400 °C, indicating that the Mn-HZSM-5 zeolite catalyst has high selectivity for HCl, which may be due to the strong acidity of the Mn-HZSM-5 zeolite catalyst and the presence of abundant B acid on the surface. The HCl production rate of the Cr-HZSM-5 zeolite catalyst was second only to that of the Mn-HZSM-5 zeolite above 400 °C and higher than that of the other catalysts, which shows that an appropriate acidity is conducive to the production of HCl. The CO_2 production rates of Cr-HZSM-5 and Mn-HZSM-5 were relatively high, high oxidation led to the formation of more Cl_2. However, Co-HZSM-5, Cu-HZSM-5 and Fe-HZSM-5 molecular sieves and HZSM-5 molecular sieve catalysts did not detect Cl_2 in the catalytic DCM products. The Cr-doped HZSM-5 catalysts formed the most oxygen vacancies, and the contents of surface adsorbed oxygen and surface lattice oxygen were higher than those of the other catalysts. Lattice oxygen with mobility diffused to the outer surface of the catalyst, replacing Cl species adsorbed on the oxygen vacancies and promoting the formation of Cl_2,[58] and its Cl_2 production rate was also the highest. In addition, the Cl_2 production temperature of Cr-HZSM-5 was 300 °C, which was lower than that of Mn-HZSM-5 because Cr-HZSM-5 has more surfactant active oxygen components. The Cl_2 production temperature of Mn-HZSM-5 was 400 °C, which increased the Cl_2 generation temperature. Fe-HZSM-5 did not produce Cl_2. Combined with the Cl balance, these results indicate that Fe-HZSM-5 also has good HCl selectivity.

From the perspective of CO_2 selectivity (Fig. 6(f)) and intermediate products (Fig. 6(h)), all the metal-doped molecular sieve catalysts had higher CO_2 selectivity than do the HZSM-5 molecular sieve catalysts during initial catalysis, but when the temperature was higher than 250 °C, the CO_2 selectivity of all the catalysts began to decrease to varying degrees. Mn-HZSM-5 exhibited high CO_2 selectivity, whereas the CO_2 selectivity of the HZSM-5 molecular sieve catalysts first increased but then decreased, whereas the intermediate organic byproducts of the HZSM-5 molecular sieve catalysts first decreased and then increased. This was mainly because HZSM-5 has low redox properties, resulting in many organic byproducts that cannot be deeply oxidized, covering the activity centre and reducing the oxidation performance. Metal Cr- and Mn-doped zeolite catalysts resulted in fewer intermediate organic byproducts and higher CO_2 selectivity, indicating that metal Cr- and Mn-doping enhanced the redox properties of the catalysts. However, on the basis of this data and the catalytic activity data and CO_2 and CO yield data, compared with Mn-HZSM-5, Cr-HZSM-5 had a lower catalytic activity, CO_2 yield and selectivity but a higher CO generation capacity and fewer organic byproducts (350–450 °C range), which was related to the strong acidity of Cr-HZSM-5, the presence of more acid sites and relatively high reduction temperatures.

During DCM degradation, CH_3Cl was the only byproduct detected. Fig. 6(g) shows that the Mn-HZSM-5, Co-HZSM-5, Fe-HZSM-5 and HZSM-5 zeolite catalysts produced CH_3Cl during the catalytic oxidation of DCM. Notably, the production rate of the Mn-HZSM-5 zeolite catalyst CH_3Cl first tended to increase but then tended to decrease in the range of 250–450 °C. The yield of CH_3Cl reached a maximum of 20% at 350 °C, and CH_3Cl was almost undetectable at 400 °C. In addition, the CH_3Cl yields of Co-HZSM-5 and HZSM-5 began to decrease at 350 °C and 400 °C, respectively. Some scholars believe that DCM first reacts with OH species on the surface of the catalyst to continuously deCl to produce HCl and simultaneously forms HCHO intermediates. HCHO intermediates generate methoxy groups and formate through disproportionation reactions, the formate species are further oxidized to COx, and the reactions of methoxy groups and HCl can generate CH_3Cl.[39] The above results show that at lower temperatures, DCM can be catalysed by strong acids on molecular sieves to produce more methoxy species and HCl, and these components can react to generate CH_3Cl. As the temperature increases, the activity of surface oxygen species gradually increases, and the intermediate products are further oxidized, so the production rate of CH_3Cl decreases. In addition, when the temperature increases, the surface acid site cracking ability is increased, which strengthens the dechlorination of CH_3Cl, thereby weakening the production ability of CH_3Cl. No CH_3Cl was detected in the catalytic oxidation products of DCM on the Cr-HZSM-5 and Cu-HZSM-5 catalysts, indicating that after Cr and Cu doping, the surface oxygen activity is relatively high at low temperatures, which effectively inhibits the generation of CH_3Cl; furthermore, this result shows that Cr-HZSM-5 has relatively strong acidity and more acid sites, which improves the dechlorination of CH_3Cl and weakens the generation ability of CH_3Cl.

As shown in Fig. 6(h) and (i), the chlorine-containing intermediate products of the HZSM-5 molecular sieve were much more abundant than those of the other metal-doped molecular sieve catalysts were, and there were more intermediate organic byproducts. This was likely because at 100–250 °C, owing to the acid site of the molecular sieve catalyst, DCM was quickly adsorbed at the activecentre, and the C–Cl bond broke, producing many intermediate products. Furthermore, the intermediate products reacted with Cl to form chlorine-containing intermediate products. Since the low degree of oxidation of HZSM-5 was not sufficient to oxidize other organic byproducts and chlorine-containing intermediate products

produced by DCM catalytic degradation, the intermediate products produced by HZSM-5 were much greater than those produced by metal-doped molecular sieves. In addition, the Cl component on the surface of the HZSM-5 molecular sieve reached a high value at 250 °C and then decreased, and HCl was produced (Fig. 6(e)). The surface organic byproducts also began to decrease, which proved that the active platform of HZSM-5 between 200–250 °C was caused by the deposition of Cl components (including HCl, Cl atoms, organochlorine, *etc.*) and intermediate nonchlorine organic transition products, which were not removed in time. At higher temperatures, the formation rates of Cr-HZSM-5 and Mn-HZSM-5 intermediate organic products and chlorine-containing byproducts were lower, indicating that the coupling of Cr and Mn can promote less carbon deposition and chlorine deposition in ZSM-5 molecular sieves, which is related to their strong redox ability and acidity. Combined with the results of the HCl, Cl_2 and CH_3Cl yields, the metal-coupled HZSM-5 exhibited a higher Cl removal ability and improved the chlorine poisoning resistance of ZSM-5, which was consistent with the SEM-EDS results. Except for Cu-HZSM-5, at 350–450 °C, the amount of surface-deposited chlorine on Mn-HZSM-5, Co-HZSM-5, Cr-HZSM-5 and Fe-HZSM-5 was relatively low, and the amount of surface-deposited chlorine on Cr-HZSM-5 was significantly less than that on the other catalysts, indicating that Cr-HZSM-5 had better resistance to chlorine poisoning. Before 450 °C, a certain amount of chlorine was deposited on Mn-HZSM-5, and before 450 °C, less chlorine deposition was observed, indicating that Mn-HZSM-5 can achieve better chlorine resistance at high temperatures, which is related to the synergy between its increased surface acidity and enhanced redox properties at high temperatures.

Fig. 6(j) shows the catalytic degradation rate curves of DCM at 360 °C for different catalysts. The degradation rate obtained with HZSM-5 decreased rapidly with increasing time, and although the catalytic activity of all the metal-doped zeolites decreased, the downwards trend was significantly smaller than that of undoped HZSM-5. The initial catalytic activities of Cr-HZSM-5 and Mn-HZSM-5 were high, but with increasing catalytic time, the catalytic activity of Mn-HZSM-5 gradually decreased, while Cr-HZSM-5 exhibited good catalytic stability. Therefore, transition metal doping can improve the chlorine resistance and carbon deposition resistance of zeolite catalysts.

The oxidation process of CVOCs is generally divided into two stages. First, the C–Cl bonds of CVOCs are adsorbed, activated and fractured at the acid centres on the catalyst surface and combine with H^+ in Brønsted acids to generate HCl. When Cl combines with a Lewis acid, Cl_2 is generated *via* the migration and replacement of peripheral oxygen components, and the intermediate organic products undergo deep oxidation at the oxidation site, finally generating COx, HCl, Cl_2 and H_2O. Therefore, the acidic sites and redox properties of the catalyst are the two key factors for the adsorption and subsequent oxidation of CVOCs.[59,60] The above redox performance results showed that the *in situ* introduction of metals jointly changed the acidity and redox properties of the catalyst and that, as a result, good synergy between them is conducive to improving the catalytic activity of the catalyst for CVOCs.

Furthermore, the above catalytic results indicate that the *in situ* introduction of metals improved the acidity and redox properties of the ZSM-5 catalysts. However, the strength of a single oxidative activity or acidity parameter and the order of catalytic activity were not consistent, and the better the synergistic effect of acidity and reducibility was, the higher the catalytic activity was. Although the Mn-HZSM-5 catalyst has higher catalytic activity and CO_2 selectivity than the Cr-HZSM-5 catalyst does, it generates a large amount of CH_3Cl in the catalytic oxidation process of DCM, and the stability, surface resistance to chlorine deposition and carbon deposition of the Mn-HZSM-5 molecular sieve catalyst are weaker than those of Cr-HZSM-5; however, both catalysts can exhibit higher HCl selectivity. In addition, Cr-HZSM-5 has a better ability to remove oxygen vacancy Cl, a better product distribution and better chlorine resistance and carbon deposition resistance due to its abundant surface acid sites, surface lattice oxygen species and surface adsorbed oxygen species and relatively high low-temperature reducibility, which indicates a better balance between acidity and reducibility.

To further strengthen innovative research, the catalytic performance of some catalysts prepared by other researchers were listed out for better comparison with the catalysts in this work. As shown in Table S2, compared with supported catalysts (such as 9% Cr/HZSM-5, 1% Cr-O/HZSM-5 and so on), the T_{90} of 0.5% Cr-HZSM-5 and 0.5% Mn-HZSM-5 decreased from 500 °C to 405 °C and 360 °C with a higher airspeed (80000 h^{-1}), respectively. The decline of T_{90} of catalysts in this work were much greater than those of others. Moreover, the T_{90} of 0.5% Cr-HZSM-5 and 0.5% Mn-HZSM-5 were close to core–shell structure catalyst (such as Mn–Co@Z) and ZSM-5 supported noble metal (such as 0.01 Pt/HZSM-5) with a relative airspeed of approximately 5.3 times. The above results indicate that the doped ZSM-5 prepared in this work possesses a better catalytic performance.

To further examine the durability of M-HZSM-5 catalysts, the reuse experiments of Cr-HZSM-5 and Mn-HZSM-5 catalysts were done. To be sure, before catalytic testing, the catalysts were calcined to clear surface organic carbon. The fifth cycle catalytic testing curves of Cr-HZSM-5 and Mn-HZSM-5 are shown in Fig. S4. From that, after fifth cycle, the catalytic performance has slightly decreased, however, the catalyst could maintain a high catalytic activity.

3.3 Analysis of anti-carbon deposition and anti-chlorine properties

In the process of catalytic oxidation, the products of incomplete oxidation may remain on the surface of the catalyst, resulting in chlorine and carbon deposition on the surface of the molecular sieve.[61] To investigate the effects of metal atom doping on the anti-chlorine and anti-carbon deposition properties of molecular sieve catalysts, three catalysts with better catalytic performance, Cr-HZSM-5, Mn-HZSM-5, Co-HZSM-5 and HZSM-5, were catalysed at 360 °C for 12 hours. Thermogravimetric analysis

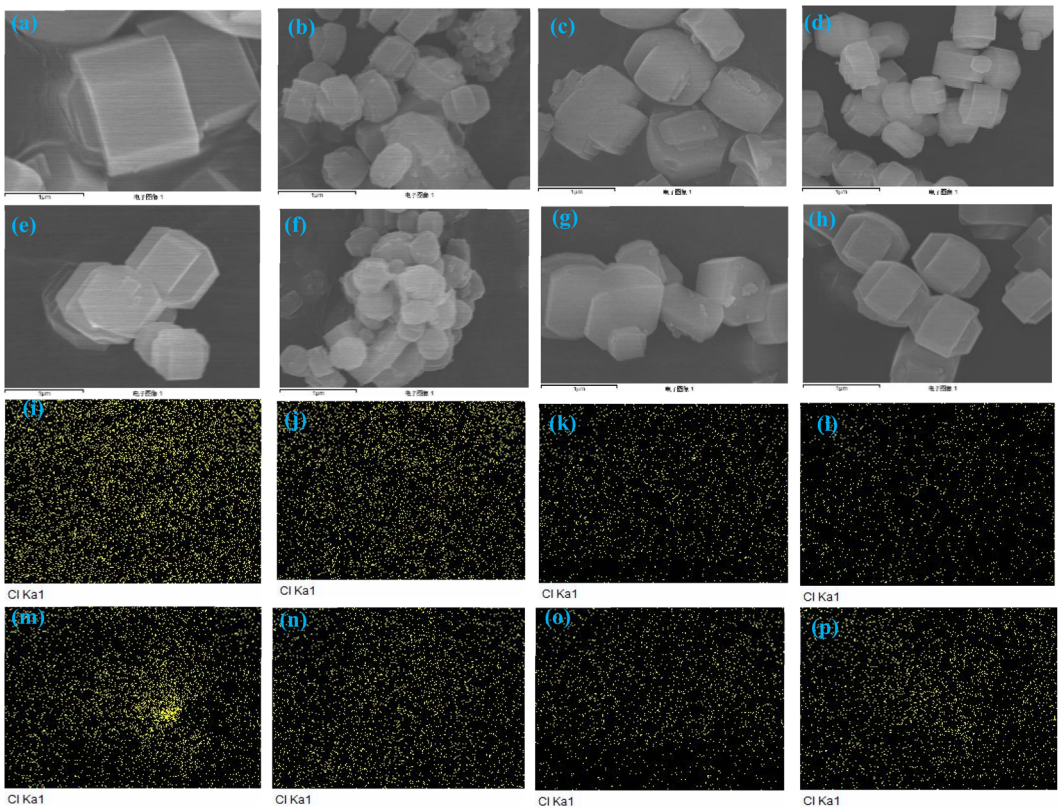

Fig. 7 The SEM images and EDS-Cl diagrams of each catalyst before and after the catalytic reaction. (a–d) SEM images of HZSM-5, Cr-HZSM-5, Mn-HZSM-5 and Co-HZSM-5 before the reaction. (e–h) SEM images of HZSM-5, Cr-HZSM-5, Mn-HZSM-5 and Co-HZSM-5 after the reaction. (i–l) EDS-Cl diagrams of HZSM-5, Cr-HZSM-5, Mn-HZSM-5 and Co-HZSM-5 before the reaction; (m–p) EDS-Cl diagrams of HZSM-5, Cr-HZSM-5, Mn-HZSM-5 and Co-HZSM-5 after the reaction.

and energy spectrum scanning analysis of surface Cl were performed. Fig. 7(a–d) shows the surface morphology of each catalyst before catalysis, Fig. 7(e–h) shows the surface morphology of each catalyst after catalysis, Fig. 7(i–l) shows the distribution of the surface Cl of each catalyst before catalysis, and Fig. 7(m–p) shows the distribution of the surface Cl of each catalyst after catalysis. Fig. 7(a–h) shows that the morphology of the catalysts consisted of regular hexagonal particles 0.5∼1 μm in size. Before and after the catalytic reaction, the apparent morphology of the catalysts did not change significantly, and there was no obvious accumulation of impurities on the surface. This shows that the catalysts have good thermal stability and are not easy to sinter and deactivate under high-temperature reflection. Fig. 7(i–p) shows that the surface Cl distributions of the Mn-HZSM-5 and Cr-HZSM-5 catalysts did not change significantly before and after the catalytic reaction, whereas the surface of the HZSM-5 catalyst showed obvious yellow bright spots, and the Cl on the surface of the Co-HZSM-5 catalyst also increased slightly, indicating that there was a large accumulation of Cl on the surface of the HZSM-5 molecular sieve catalyst. Combined with the production rates of the chlorine-containing byproducts of each catalyst in Fig. 6(i), the Mn-HZSM-5 and Cr-HZSM-5 catalysts promoted the decomposition and oxidation of chlorine-containing organic compounds during the catalytic process because of their strong acidity and oxidation ability; at the same time, these catalysts improved the ability of surface Cl to be removed in the form of HCl and Cl_2, greatly reduced the deposition of chlorine on the surface of the molecular sieve catalyst, and improved the chlorine resistance. A comparison of the chlorine accumulation before and after catalysis of the four catalysts revealed that the coupling of the metals Cr, Mn and Co can increase the chlorine resistance of the molecular sieve catalyst and reduce the occurrence of deactivation due to Cl poisoning during the catalyst process,[62] which is consistent with the results of the previous section. Additionally, the SEM images of Cr-ZSM-5 after the reuse studies was also characterized, as shown in Fig. S5, which display that there was almost no change between after the fifth cycle.

Another main reason for the deactivation of molecular sieve catalysts is the generation of carbon deposits on the surface. HZSM-5 sieves are highly acidic and undergo weak self-oxidation. The intermediate transition products cannot be completely oxidized in time and are prone to polymerization and chain growth. Carbonaceous precipitation occurs in the micropores of the molecular sieve, which blocks the active-centres and pores, resulting in a decrease in the catalytic activity of the molecular sieve catalyst.[63] Fig. 8 shows the TG curves of HZSM-5, Co-HZSM-5, Cr-HZSM-5 and Mn-HZSM-5 before and after catalysis at 200–450 °C. The weight loss of 3–6% of all the catalysts in the range of 100–200 °C should be attributed to the

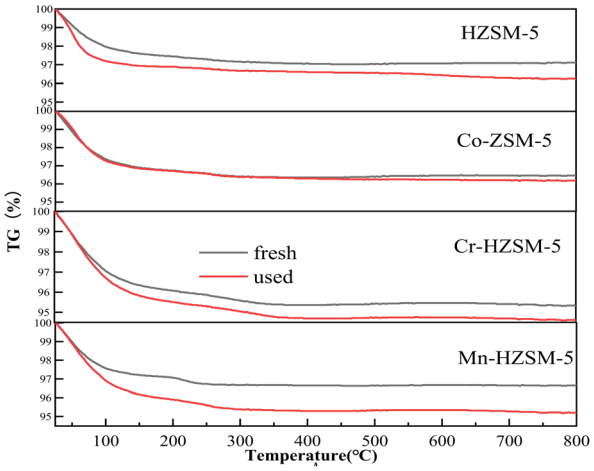

Fig. 8 TG curves of the catalysts in air.

physical adsorption of water on the catalyst surface. The weight loss phenomenon at 200–500 °C is attributed to carbon deposition on the catalyst surface and the combustion decomposition of other macromolecular substances adsorbed. The weight loss above 500 °C was due to the loss of water in the lattice of the molecular sieve.[64] The figure shows that the weight loss rate of all the catalysts after the catalytic reaction was greater than that before the catalytic reaction, but the difference in weight loss rate before and after catalysis was within the range of 1–2%, indicating that all the catalysts have less surface carbon deposition during the catalytic process; this is consistent with the results of the production rate of intermediate organic byproducts of each catalyst in Fig. 6(h).

3.4 Reaction path of surface reactive oxygen

To study the difference in catalytic performance between metal-coupled ZSM-5 and metal-supported ZSM-5, a zeolite catalyst with a metal doping content of 1.2% was prepared by hydrothermal synthesis, and a supported ZSM-5 zeolite catalyst with a metal content of 1.2% was prepared by impregnation. In this study, 1.2% Cr-HZSM-5 and 1.2% Cr/HZSM-5 were selected as the research objects and analysed *via* NH_3-TPD to assess the surface acidity. The results are shown in Fig. 9. The total acid content of the 1.2% Cr/HZSM-5 zeolite catalyst was less than that of the 1.2% Cr-HZSM-5 zeolite catalyst because the active metal species loaded on the surface covered the acid sites on the surface, making the zeolite less acidic. The moderate-strength acid content of the 1.2% Cr/HZSM-5 catalyst was significantly lower than that of the 1.2% Cr-HZSM-5 catalyst, and there were no strong acid sites. Compared with the 1.2% Cr-HZSM-5 catalyst, the 1.2% Cr-HZSM-5 catalyst had more moderate-strength acid and strong acid sites.

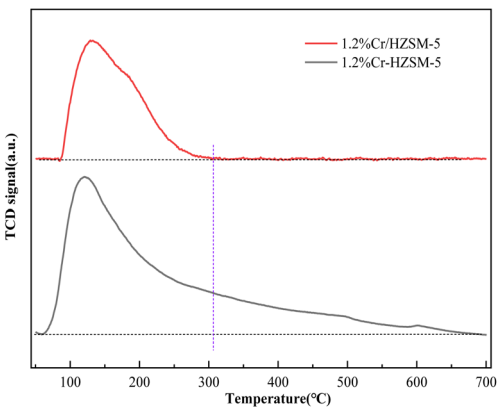

Fig. 9 NH_3-TPD diagrams of zeolites prepared with different metal modification methods.

As shown in Fig. 10, below 300 °C, the catalytic activity of 1.2% Cr-HZSM-5 was significantly greater than that of 1.2% Cr/HZSM-5, indicating that 1.2% Cr-HZSM-5 had high low-temperature activity. This high activity is related to its strong surface acidity, mainly because Cr^{6+} replaces Si^{4+}, and after hydrogenation, more surface Brønsted acids can be produced, which improves the adsorption and cleavage of DCM. Above 300 °C, the catalytic activity curves of 1.2% Cr-HZSM-5 and 1.2% Cr/HZSM-5 almost coincided, indicating that the two catalysts had similar DCM catalytic activities at higher temperatures. However, the CO_2 production rate of the 1.2% Cr-HZSM-5 was significantly greater than that of the 1.2% Cr/HZSM-5, and the CO yield was similar, indicating that the metal-coupled 1.2% Cr-HZSM-5 had a higher DCM deep oxidation capacity than did the metal-supported 1.2% Cr/HZSM-5. Furthermore, the results suggested that different modification methods had different effects on the acidity and redox properties of the zeolite catalysts and that Cr coupling could synergistically change the surface acidity and redox properties of the catalysts. Moreover, metal ion doping improved DCM adsorption, cleavage and oxidation capacity at low and high temperatures. In addition, the HCl and Cl_2 yields of 1.2% Cr-HZSM-5 were significantly greater than those of 1.2% Cr/HZSM-5, indicating that 1.2% Cr-HZSM-5 had a relatively high Cl removal ability and high chlorine resistance. The yield of HCl from 1.2% Cr/HZSM-5 tended to decrease above 400 °C, possibly because the active components on the surface of the supported catalyst covered the acidic sites on the surface of the zeolite surface, which weakened the acidity of the catalyst surface and thus greatly weakened the removal of HCl. HCl may also combine with surface Cr to form chloride or chlorine oxides, which could explain why the Cl removal capacity of 1.2% Cr/HZSM-5 was lower than that of 1.2% Cr-HZSM-5.

Although HZSM-5 showed similar catalytic activity at higher temperatures, it can be concluded from the distribution of catalytic products that the supported catalyst (1.2% Cr/HZSM-5) had a lower CO_2 production rate and chlorine-containing inorganic product production rate than did the doped catalyst (1.2% Cr-HZSM-5). In this work, the surface Cl distribution of the catalyst before and after the reaction was characterized. Fig. 11 shows the SEM-EDS diagram of surface Cl on the ZSM-5 molecular sieve catalyst modified with Cr before and after the reaction. The change in surface Cl species was not obvious before and after the doping-modified molecular sieve catalysis, whereas the supported molecular sieve catalyst showed dense enrichment of Cl on the surface after the catalytic reaction. The 1.2% Cr-HZSM-5 molecular sieve contained a large amount of acid, which was helpful for the preliminary cleavage and

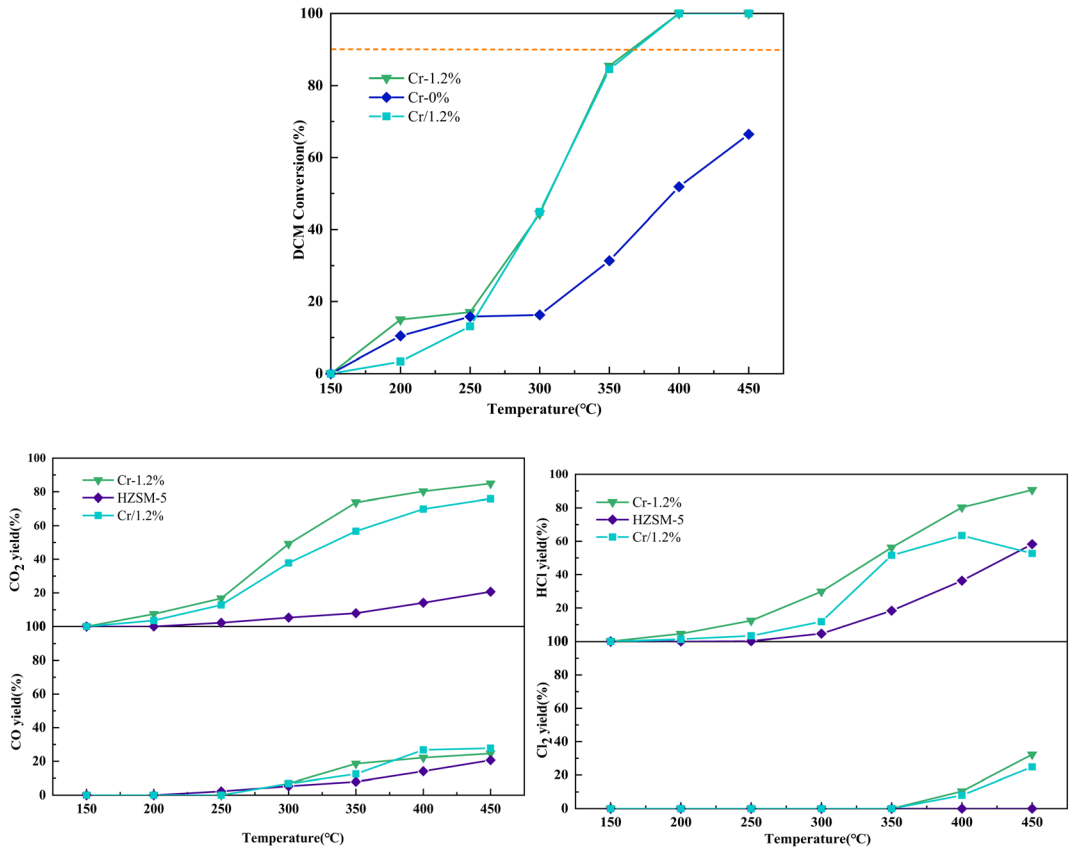

Fig. 10 Catalytic efficiency and product distribution of HZSM-5 zeolite catalysts prepared with different metal modification methods.

subsequent oxidation of C–Cl in CVOCs so that the surface Cl species could be removed from the catalyst surface. However, the surface acidity of the 1.2% Cr/HZSM-5 molecular sieve catalyst was weak, which was not conducive to the removal of surface Cl, resulting in dense adsorption on the catalyst surface.[48] This is also consistent with the result that the production rate of HCl on the 1.2% Cr/HZSM-5 molecular sieve tended to decrease above 400 °C. It can also be seen from the total energy spectrum that the content of Cr in the catalyst before and after the catalytic reaction of the 1.2% Cr-HZSM-5 molecular sieves is less different, indicating that the loss of Cr during the reaction is lower.

Furthermore, compared with the loadable chromium/HZSM-5 catalyst, the reason why the redox performance of the doped chromium HZSM-5 can be significantly enhanced is not only the many oxygen vacancies generated but also the migration path of surface oxygen species being shortened; that is, the reactive surface oxygen species can migrate to the adsorption site of organic components or organic transition state compounds and attack the organic components in less time. However, the reactive surface oxygen of supported catalysts migrates from supported metal oxides to the adsorption site on the carrier surface, which takes a relatively long time, prevents some organic components from being oxidized in a timely manner leads to some organic byproducts being generated and decreases the catalytic performance. In addition, many Cl species can be also deposited on the surface of catalysts. The reflection schematic is shown in Fig. 12.

3.5 Catalytic oxidation mechanism and chlorine resistance mechanism

It is generally believed that DCM catalytic oxidation mainly occurs through two processes: first, DCM binds to the surface acid site on the catalyst surface, and dechlorination occurs; the generated organic transition products can be gradually oxidized to CO_2 and H_2O by the surface oxygen component, while the chlorine component can combine with hydrogen to form HCl or Deacon reactions to form Cl_2. Pinard *et al.*[65] studied the catalytic oxidation process of DCM on H-type molecular sieves (HFAUs) and reported that the catalytic oxidation mechanism of DCM on H-type molecular sieves is similar to the catalytic degradation mechanism of DCM on γ-Al_2O_3 proposed by Brink,[66] both of which are surface hydroxyl groups of the catalyst that play a major role. The difference is that when DCM is catalysed on the HFAU molecular sieve, the formate species on the catalyst surface are more likely to generate CHOH and CO during the reaction process, and further oxidization to CO_2 is difficult. Maupin *et al.*[67] prepared an Al_2O_3 catalyst containing only L acid sites and investigated the catalytic degradation of DCM on this sample: First, the Cl atom in DCM adsorbs on the oxygen vacancy on the surface of Al_2O_3, and the activation of the C–Cl bond occurs simultaneously; then, under the action of lattice

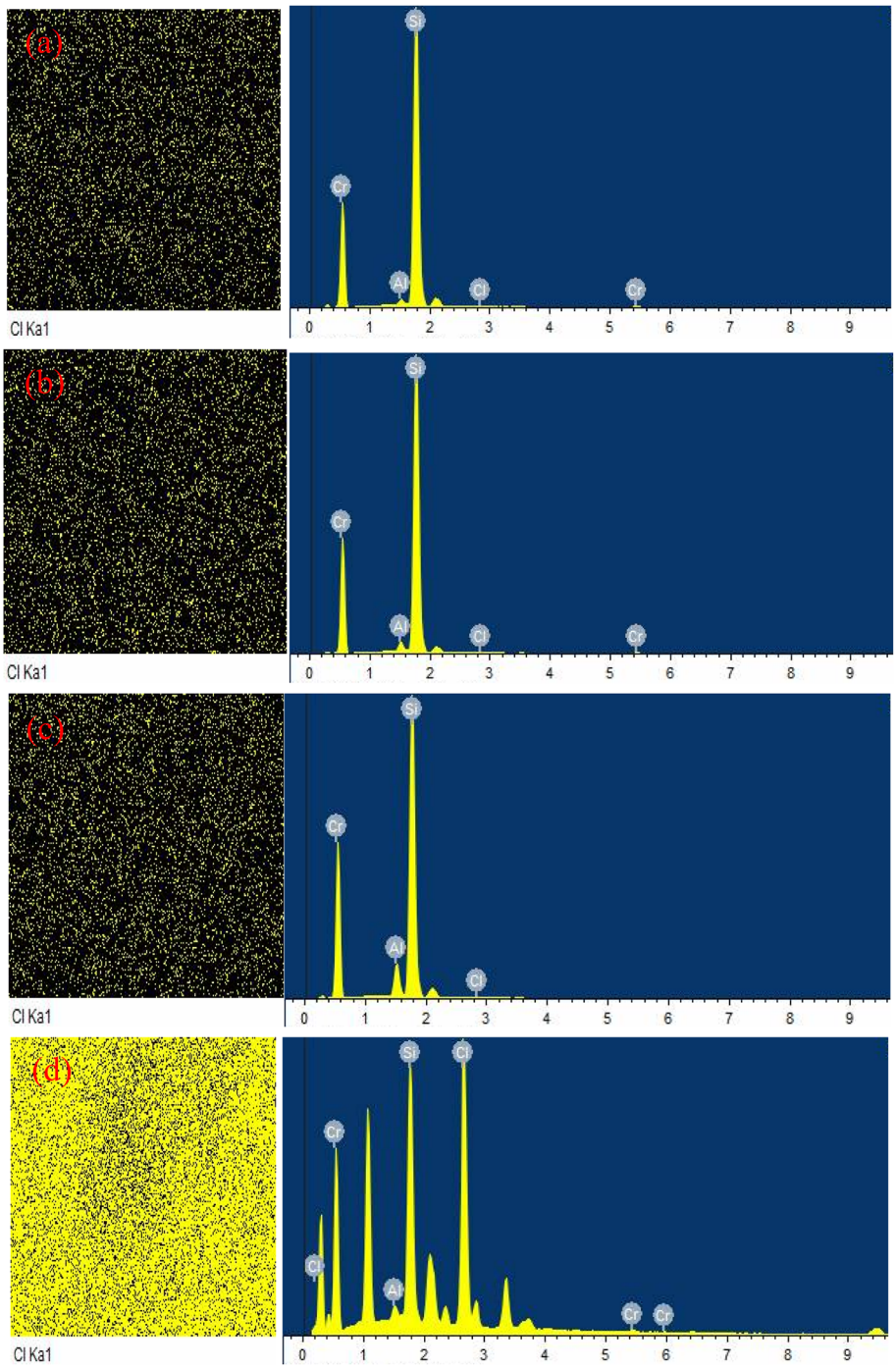

Fig. 11 EDS-Cl images of (a) fresh 1.2% Cr-HZSM-5, (b) used 1.2% Cr-HZSM-5, (c) fresh 1.2% Cr/HZSM-5 and (d) used 1.2% Cr-HZSM-5.

oxygen, the C–Cl bond is broken to form CH_3Cl and chloromethoxy species on the catalyst surface; and finally, additional reactions generate chloromethyl species and formate species and generate CO and CO_2. In combination with the results of previous studies, the transition metal-coupled ZSM-5 catalyst prepared in this paper has only CH_3Cl found in the Mn, Co-HZSM-5 and HZSM-5 catalysts during the catalytic oxidation of DCM, and no other organochlorine byproduct gases have been detected. Certain amounts of CO_2, CO and HCl were found in the products of each catalyst, and Cl_2 was detected in the products of Cr, Mn-HZSM-5 at higher temperatures. In addition, there are more B acids and L acids on the surface of M-HZSM-5 at the same time. Combined with previous research results, the decomposition and oxidation of DCM on M-HZSM-5 catalysts can be inferred in Fig. 13 and 14.

As shown in Fig. 13 and 14, dichloromethane can be adsorbed and activated by Lewis and Brønsted acids on the surface of M-HZSM-5 (where M represents the metal), resulting in the C–Cl bond breaking. The generated Cl atoms can combine with metal ions or react with the H protons provided by Brønsted acids to

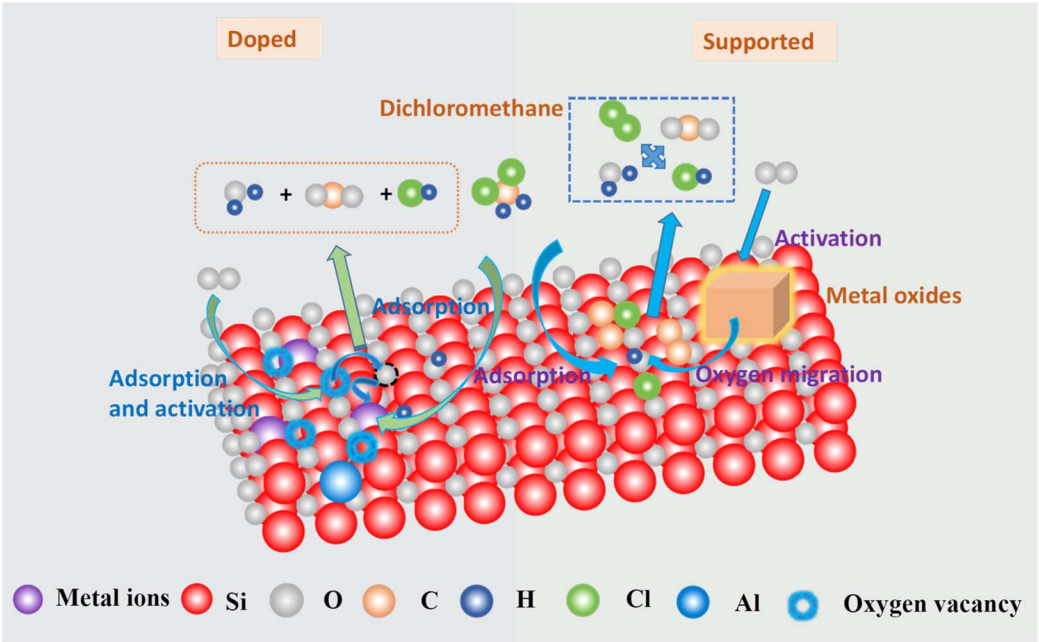

Fig. 12 Schematic diagram of the catalytic oxidation of DCM over ZSM-5 doped and loaded with transition metals.

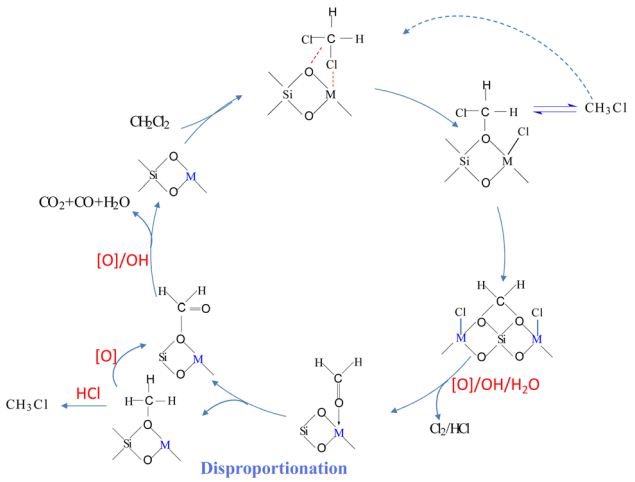

Fig. 13 The reaction mechanism of DCM over M-HZSM-5 with Lewis acids.

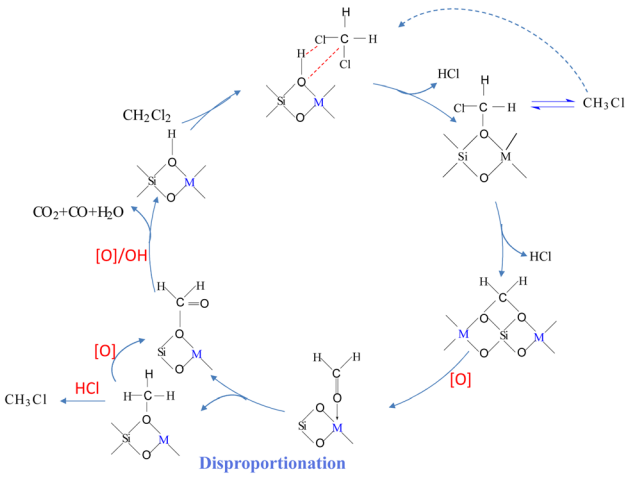

Fig. 14 Reaction mechanism of DCM over M-HZSM-5 with Brønsted acids.

form HCl and then desorb. Furthermore, the generated chloromethoxy groups can undergo dechlorination or react with H to form CH_3Cl. CH_3Cl can be adsorbed and activated by surface acidic sites for subsequent oxidation. After dechlorination of the chloromethoxy groups, hemiacetal substances are formed. The Cl atoms occupying the Lewis sites can be replaced by surface active oxygen components and removed in the form of Cl_2. Hemiacetal substances can be further oxidized to formaldehyde, and formaldehyde can generate methoxy and formate substances through disproportionation reactions. Under certain conditions, methoxy groups can react with HCl to form CH_3Cl, which can also generate formate substances under the attack of surface-active oxygen components. The formate substances are further oxidized to carbonates and finally generate CO_2, CO and H_2O. Moreover, CO is also deeply oxidized to CO_2 by surface oxygen components. By strengthening the mobility and reducibility of the surface oxygen components of the catalyst, as well as maintaining appropriate surface acidity and synergistically increasing the redox ability and the synergy of surface acidity, the catalytic activity and deep oxidation ability of DCM can be improved, and the generation of CH_3Cl and other chlorine-containing organic byproducts can be reduced or even avoided.

4. Conclusion

In this work, a doped M-HZSM-5 zeolite catalyst was successfully synthesized by hydrothermal synthesis to explore the

effects of different types of transition metal ion doping on the physicochemical properties, catalytic performance, reactive oxygen species, reaction mechanism and reaction pathway of DCM oxidation. Several conclusions can be drawn as follows:

(1) Transition metal doping can synergistically modify the surface acidity and redox capability of HZSM-5 molecular sieves, increasing their catalytic activity, chlorine resistance, and stability for DCM oxidation. Cr-HZSM-5 and Mn-HZSM-5 exhibited good catalytic activity. Mn-HZSM-5 showed higher CO_2 selectivity and HCl yield; however, it generated some CH_3Cl during the catalytic oxidation of DCM. Cr-HZSM-5 demonstrated outstanding stability, high HCl selectivity, and effective removal of chlorine from oxygen vacancies, which was attributed primarily to its abundant surface acid sites and active oxygen species. However, Cr-HZSM-5 also produced some CO. Furthermore, these results indicate that synergistically improving the surface acidity and redox performance, while optimizing their compatibility, is essential to simultaneously increase the catalytic activity for DCM, deep oxidation capacity, HCl selectivity, and resistance to chlorine poisoning.

(2) Components doped with 1.2% Cr-HZSM-5 have more strongly acid sites than those doped with 1.2% Cr/HZSM-5 do and exhibit higher DCM catalytic activities for 1.2% Cr-HZSM-5 than for 1.2% Cr/HZSM-5 at low temperatures. At high temperatures, the two have similar DCM catalytic activities. Compared with the supported catalyst, the doped catalyst can significantly increase the yield of CO_2 and HCl, and the Cl chloride deposition on the surface of the catalyst after the reaction is significantly lower than that of the supported catalyst, which improves the chlorine resistance. The migration path of surface oxygen species can be shortened over M-HZSM-5, which can significantly enhance the redox properties.

(3) The synergistic reaction mechanism of surface active oxidation components and surface B/L acid sites can be intensified because of the fast interaction between the lattice transition metal atom (as the acidic adsorption site) and the surface reactive oxygen (generated by the lattice doping of transition metals) for DCM oxidation over doped ZSM-5 with the lattice Si^{4+} ions anchored *in situ* by transition metal atoms. This can facilitate deep oxidation and HCl selectivity. Additionally, synergistic reaction routes are also proposed in this paper.

(4) The synergistic reaction pathway between surface acidity and redox properties and the surface oxygen migration rate will be studied by DFT in the future.

Conflicts of interest

The authors declare that they have no known competing financial interests or personal relationships that could have influenced the work reported in this study.

Data availability

The data supporting this article have been included within the manuscript and as part of the supplementary information (SI). Supplementary information is available. See DOI: https://doi.org/10.1039/d5ra06126a.

Acknowledgements

This work was supported by the National Key R & D Program "Research and Demonstration of Regional Coordinated Prevention and Control Refined Governance Technology Solutions"; Implementation Period: December 2024 to December 2027; Project Number: 2024YFC3713405.

References

1 L. Wu, Y. Zhu, J. Yuan, X. Guo and Q. Zhang, *J. Mater. Sci. Chem. Eng.*, 2024, **12**, 1–43.
2 S. Yun, F. Kaixuan, P. Caihong, Z. Yanfei, S. Chunfeng, J. Na, M. Degang, L. Xuebin, L. Caixia, H. Rui and L. Qingling, *Environ. Sci. Technol.*, 2022, **56**(14), 9854–9871.
3 B. Xie, Z. Wang, X. Zhang, M. Ding, M. Li, X. Guo, Q. Dai, L. Wang, W. Zhan, Y. Guo, A. Wang and Y. Guo, *Sep. Purif. Technol.*, 2024, **345**, 127428.
4 H. Lin, Y. Liu, J. Deng, L. Jing, Z. Wang, L. Wei, Z. Wei, Z. Hou, J. Tao and H. Dai, *Catalysts*, 2024, **14**, 531.
5 W. Peng, J. Xiaojing, Q. Yongcai and Y. Daiqi, *Environ. Sci. Technol.*, 2021, **55**(8), 4268–4286.
6 S. Yijun, W. Jialu, W. Yiyan, K. Fanzhe and Z. Renxian, *J. Environ. Chem. Eng.*, 2022, **10**, 107629.
7 W. Shan, X. Ping, Y. Jie, A. C. Carabineiro Sónia, W. Marek, Z. Junjiang and L. Xinying, *Front. Chem. Sci. Eng.*, 2023, **17**, 1649–1676.
8 X. Zha, C. Yang, X. Huang, J. Ding and Z. Ding, *Environ. Pollut. Bioavailability*, 2024, 36.
9 Z. Zhiwei, L. Qianqian, S. Guijin, P. Jiaxin, S. Bohua, M. Jing and S. Bin, *J. Environ. Sci.*, 2024, **138**, 326–338.
10 B. Miranda, E. Díaz, S. Ordóñez, A. Vega and F. V. Díez, *Appl. Catal., B*, 2005, **64**, 262–271.
11 L. Wenjun, Z. Yuxue, R. Sida and S. Xiujuan, *Chem. Phys.*, 2023, **566**, 111787.
12 G. Long, M. Chen, Y. Li, J. Ding, R. Sun, Y. Zhou, *et al*, *Chem. Eng. J.*, 2019, **360**, 964–973.
13 X. Zhang, L. Dai, Y. Liu, J. Deng, L. Jing, X. Yu, Z. Han, K. Zhang and H. Dai, *Catal. Sci. Technol.*, 2020, **10**, 3755–3770.
14 W. Shixing, Z. Haijun, X. Yuntai, T. Zhicheng and Z. Jiyi, *Sci. Total Environ.*, 2023, **860**, 160472.
15 Z. Nini, G. Yanglong, G. Yun, D. Qiguang, W. Li, D. Sheng and Z. Wangcheng, *Chem. Eng. J.*, 2023, **454**, 140391.
16 X. Xie, S. Xu, F. Chen, X. Zhan and D. g. Cheng, *Chem. Eng. Sci.*, 2025, **301**, 120763.
17 Z. Zhang, S. Ma, H. Zhao, Y. Hu, B. Avid and S. Xue, *Fuel*, 2025, **384**, 134048.
18 A. Aranzabal, M. Romero-Sáez, U. Elizundia, J. R. González-Velasco and J. A. González-Marcos, *J. Chem. Technol. Biotechnol.*, 2016, **91**, 318–326.
19 A. Aranzabal, M. Romero-Sáez, U. Elizundia, J. R. González-Velasco and J. A. González-Marcos, *J. Catal.*, 2012, **296**, 165–174.
20 S. Scirè, S. Minicò and C. Crisafulli, *Appl. Catal., B*, 2003, **45**, 117–125.

21 B. d. Rivas, C. Sampedro, E. V. Ramos-Fernández, R. López-Fonseca, J. Gascon, M. Makkee and J. I. Gutiérrez-Ortiz, *Appl. Catal., A*, 2013, **456**, 96–104.
22 Y. Su, K. Fu, Y. Zheng, N. Ji, C. Song, D. Ma, X. Lu, R. Han and Q. Liu, *Appl. Catal., B*, 2021, **288**, 119980.
23 P. Sun, S. Zhai, J. Chen, J. Yuan, Z. Wu and X. Weng, *Appl. Catal., B*, 2020, **272**, 119015.
24 P. Sun, W. Wang, X. Dai, X. Weng and Z. Wu, *Appl. Catal., B*, 2016, **198**, 389–397.
25 Q. Dai, W. Wang, X. Wang and G. Lu, *Appl. Catal., B*, 2017, **203**, 31–42.
26 F. Xiaoqi, C. Shuang, O. Weilong, W. Haiqiang and W. Zhongbiao, *Chin. Chem. Lett.*, 2020, **32**, 1224–1228.
27 L. Jian, Z. Jiajia, H. Jingnan, S. Yingjie, W. Fan, D. Shuang and C. Yutao, *Microporous Mesoporous Mater.*, 2022, **339**, 112004.
28 A. I. M. Smarte, O. Bilainu and I. Y. Makarfi, *Fuel Commun.*, 2024, **18**, 100101.
29 S. Boseok, K. E. Hee, K. Bogyung, P. No-Kuk, K. S. Bong, K. Dohyung and K. Minkyu, *Chem. Eng. J.*, 2023, 452.
30 J. K. Reddy, K. Mantri, S. Lad, J. Das, G. Raman and R. v. Jasra, *J. Porous Mater.*, 2020, **27**, 1649–1658.
31 M. A. Deimund, L. Harrison, J. D. Lunn, Y. Liu, A. Malek, R. Shayib and M. E. Davis, *ACS Catal.*, 2015, **6**, 542–550.
32 W. Hu, Q. Luo, Y. Su, L. Chen, Y. Yue, C. Ye and F. Deng, *Microporous Mesoporous Mater.*, 2006, **92**, 22–30.
33 F. González, C. Pesquera, A. Perdigón and C. Blanco, *Appl. Surf. Sci.*, 2009, **255**, 7825–7830.
34 C. Subrahmanyam, B. Louis, F. Rainone, B. Viswanathan, A. Renken and T. K. Varadarajan, *Appl. Catal., A*, 2003, **241**, 205–215.
35 H. Zhen, W. Juan, G. Bingying and H. Hongyun, *ACS Appl. Mater. Interfaces*, 2015, **7**, 2424–2432.
36 Z. Shi, P. Yang, F. Tao and R. Zhou, *Chem. Eng. J.*, 2016, **295**, 99–108.
37 G. Wang, H. Gao and Q. Cao, *J. Porous Mater.*, 2022, **30**, 921–936.
38 J. Guo, X. Liu, X. Wen, X. Su, Y. Chu and J. Liang, *Chem. Eng. J.*, 2024, **488**, 150924.
39 P. Yang, X. Xue, Z. Meng and R. Zhou, *Chem. Eng. J.*, 2013, **234**, 203–210.
40 R. Ao, L. Ma, Z. Guo, H. Liu, J. Yang, X. Yin and Q. Pan, *Fuel*, 2021, 305.
41 L. Liu, S. Zhang, Z. Ma and S. Zhu, *Ceram. Int.*, 2020, **46**, 19738–19742.
42 Y. Wan, Y. Xing, Z. Xu, S. Xue, S. Zhang and C. Xia, *Appl. Catal., B*, 2020, **269**, 118809.
43 C. Dong, Z. Qu, Y. Qin, Q. Fu, H. Sun and X. Duan, *ACS Catal.*, 2019, **9**, 6698–6710.
44 X. Yin, L. Shen, S. Wang, B. Wang and C. Shen, *Appl. Catal., B*, 2022, **301**, 120816.
45 A. N. Ulyanov, K. I. Maslakov, C. Martin, D.-S. Yang, S. A. Chernyak, V. Markovich and S. V. Savilov, *J. Alloys Compd.*, 2020, **820**, 153106.
46 M. Chaudhary, M. Singh, A. Kumar, Prachi, Y. K. Gautam, A. K. Malik, Y. Kumar and B. P. Singh, *Ceram. Int.*, 2021, **47**, 2094–2106.
47 H. Tian, Y. Ping, Y. Zhang, Z. Zhang, L. Sun, P. Liu, J. Zhu and X. Yang, *J. Hazard. Mater.*, 2021, **416**, 126194.
48 C. Resini, T. Montanari, L. Nappi, G. Bagnasco, M. Turco, G. Busca, F. Bregani, M. Notaro and G. Rocchini, *J. Catal.*, 2003, **214**, 179–190.
49 S. Yun, F. Kaixuan, Z. Yanfei, J. Na, S. Chunfeng, M. Degang, L. Xuebin, H. Rui and L. Qingling, *Appl. Catal., B*, 2021, **288**, 119980.
50 P. Yang, S. Zuo and R. Zhou, *Chem. Eng. J.*, 2017, **323**, 160–170.
51 L. Jian, S. Yingjie, F. Xiaoheng, S. Yun, H. Jiayu, Z. Jinwei, T. Gang and H. Jingnan, *Mol. Catal.*, 2021, 499.
52 I. V. Krylova, *Russ. Chem. Bull.*, 2002, **51**, 46–53.
53 A. F. A. Rahman, A. A. Jalil, M. Y. S. Hamid, I. Hussain, N. S. Hassan and A. H. Khoja, *Mol. Catal.*, 2022, **526**, 112370.
54 Y. Jiang, J. Gao, Q. Zhang, Z. Liu, M. Fu, J. Wu, Y. Hu and D. Ye, *Chem. Eng. J.*, 2019, **371**, 78–87.
55 H. Zhou, W. Su, Y. Xing, J. Wang, W. Zhang, H. Jia, W. Su and T. Yue, *Fuel*, 2024, **366**, 131305.
56 E. P. Reddy, B. Sun and P. G. Smirniotis, *J. Phys. Chem. B*, 2004, **108**, 17198–17205.
57 T. Heyuan, P. Yuan, Z. Yibo, Z. Zeshu, S. Liwei, L. Peng, Z. Junjiang and Y. Xiangguang, *J. Hazard. Mater.*, 2021, **416**, 126194.
58 W. L. Wang, Q. Meng, Y. Xue, X. Weng, P. Sun and Z. Wu, *J. Catal.*, 2018, **366**, 213–222.
59 W. Lifeng, S. Makoto and K. Hideo, *J. Hazard. Mater.*, 2008, **154**, 390–395.
60 W. Hao, P. Bo, Z. Runduo, C. Hongxia and W. Ying, *Appl. Catal., B*, 2020, **276**, 118922.
61 W. Tang, X. Wu and D. Li, *J. Mater. Chem. A*, 2014, **2**, 2544–2554.
62 E. Finocchio, G. Ramis and G. Busca, *Catal. Today*, 2010, **169**, 3–9.
63 W. Jinlong, Z. Pengyi, L. Jinge, J. Chuanjia, Y. Rizwangul and K. Jeonghyun, *Environ. Sci. Technol.*, 2015, **49**, 12372–12379.
64 W. Xingyi, K. Qian and L. Dao, *Appl. Catal., B*, 2008, **86**, 166–175.
65 L. Pinard, J. Mijoin, P. Ayrault, C. Canaff and P. Magnoux, *Appl. Catal., B*, 2004, **51**, 1–8.
66 R. W. van den Brink, P. Mulder, R. Louw, G. Sinquin, C. Petit and J.-P. Hindermann, *J. Catal.*, 1998, **180**, 153–160.
67 I. Maupin, L. Pinard, J. Mijoin and P. Magnoux, *J. Catal.*, 2012, **291**, 104–109.